

Parametric investigation of mini-tab for load alleviation

Master thesis

Ilias Kiat

Delft University of Technology



Parametric investigation of mini-tab for load alleviation

by

Ilias Kiat

in partial fulfillment of the requirements for the degree of

Master of Science

at the Delft University of Technology,
to be defended publicly on Monday April 29, 2024 at 09:00 AM.

Student number: 4574087
Supervisors: Prof. Jurij Sodja, Luca Marino
Thesis Committee: Prof. Joris Melkert, Prof. Alexander van Zuijlen

An electronic version of this thesis is available at <http://repository.tudelft.nl/>.

Summary

For this thesis, a new load alleviation technique is investigated called a mini-tab. These small devices are placed at the upper surface of a wing to reduce the lift generated. A series of Reynolds-Averaged Navier-Stokes (RANS) simulations were performed to examine how the most important geometrical properties affect the performance of the mini-tab in alleviating the load on the wing. The first set of simulations was performed only with 1 mini-tab placed on the wing and was parameterized in height, aspect ratio, chordwise position and spanwise position. The results have shown that by introducing the mini-tabs the aerodynamics around the wing change significantly and that it is a viable method to reduce the forces acting on a wing. It is observed that increasing the height and aspect ratio decreases the lift generated significantly. The reason for this reduction in the lift is the deceleration of the flow at the leading edge which increases the pressure at the upper surface. Downstream of the mini-tab, a larger wake is observed too with an increase of the aspect ratio and height of the mini-tab. This increases the region of separated flow and decreases the lift and increases the pressure drag.

An increase of the chordwise position decreases the lift generated by the wing but this does have diminishing results. When the mini-tab is placed around 60 percent of the chordwise position the maximum lift reduction is observed. It also shows that for an increase of the spanwise position the lift is also reduced which when looking at the trend has the same effect as an increase the height. The second set of simulations was performed with multiple mini-tabs. It is observed that placing the mini-tabs orthogonal to the wind direction may not be the most sufficient way since this will create gaps between them. If the mini-tabs were orientated however with the 20 percent chord line a much lower lift was perceived indicating an increase in the performance of the mini-tabs. ¹

¹27779 words total

1

Acknowledgements

I have done my bachelor and Masters at TU Delft. I've encountered numerous challenges, each met with the support of many individuals who have helped me in shaping my academic and personal growth. I am deeply indebted to these individuals and wish to express my gratitude to them within these pages.

First and foremost, I owe an immense debt of gratitude to my family, friends, and especially my parents, whose support and encouragement have been the bedrock upon which I built my academic pursuits. Their belief in my potential, coupled with their endless sacrifices, has made this journey possible.

In particular, I want to give my gratitude to three individuals whose guidance and mentorship have left a mark on my academic and professional career.

Luca Marino stands out as a beacon of insight and knowledge. His help was often crucial in tackling new problems and solving new solutions. I am grateful for his guidance, which has enriched the quality of my work.

I am also deeply grateful for the guidance and support provided by Adrian Eberle throughout my thesis work, particularly during the initial stages. Adrian's expertise and willingness to assist were invaluable as I navigated through the early challenges of my research. His insightful feedback and encouragement helped set a solid basis for my work and gave me the confidence to tackle complex problems.

Equally or even more deserving of my gratitude is Jurij Sodja, who had a huge impact on my academic achievements. Jurij's expertise, coupled with his commitment to mentorship, transformed not only my technical skills but also my approach to problem-solving. His ability to challenge and redirect, coupled with his insights and quick thinking, has been invaluable in shaping me into a better engineer.

Jurij's dedication to making an environment of collaboration and always pushing yourself, where students are treated as respected colleagues, has left an incredible impression on me. I am profoundly grateful for the opportunity to learn from him and for the impact he

has had on my academic and professional career.

So thank you Luca, Adrian and Jurij for everything and I hope that after this project, someday we will be working together again on future researches.

To all those who have supported me along this journey, I extend my deepest appreciation. Your belief in me has been a constant source of inspiration, and I am truly humbled by the generosity of your time, knowledge, and encouragement.

Contents

1 Acknowledgements	4
List of Figures	7
2 Introduction	11
2.1 Relevance of the Project	11
2.2 State of the art aerodynamic control systems	12
2.2.1 Flaps and ailerons	12
2.2.2 Vortex generators	12
2.2.3 Conventional and sub-scale vortex generators	14
2.2.4 Gurney flap	17
2.2.5 Mini-tab	17
2.3 Research Question(s)	18
3 Theoretical Framework of Computational Fluid Dynamics	20
3.1 RANS equations and closure problem	20
3.2 Different solutions for closure problem	23
3.2.1 Spalart-Allmaras model	23
3.2.2 $k - \epsilon$ model	24
3.2.3 $k - \omega$ model	25
3.2.4 Selection of turbulence model for mini-tab simulation	25
3.3 Boundary layer and wall function	26
3.4 Mesh quality criteria	27
4 Two-dimensional analysis of mini-tab	29
4.1 Introduction	29
4.2 Methodology	29
4.3 Geometry	30
4.4 Mesh	30
4.5 Verification	32
4.5.1 Mesh Convergence Study Clean Wing	32
4.5.2 Turbulence Model	33
4.5.3 Pressure coefficient Clean wing	33
4.5.4 Lift coefficient comparison between simulation and experiment of mini-tabs	34
4.6 Results	35
4.7 Discussion	38
5 Simulation of clean wing in 3D	39
5.1 Introduction	39
5.2 Geometry	40
5.3 Mesh	40
5.4 Verification	43
5.4.1 Mesh convergence study	43
5.4.2 Turbulence model	43
5.4.3 Validation of pressure coefficient	45

5.5	Results	45
6	Analysis of the mini-tab effects on lift and drag coefficient	48
6.1	Introduction	48
6.2	Comparative analysis of mini-tabs with varied heights and aspect ratios	49
6.3	Chordwise position of the mini-tab	58
6.4	Spanwise position of the mini-tab	59
6.5	Comparative analysis of mini-tabs at different spanwise locations with constant H/c	61
6.6	Analysis of multi-tab configuration performance	63
7	Conclusion and Recommendations for Future Research	68
7.1	Conclusion	68
7.2	Recommendation for future research	69

List of Figures

1	Vortex generators used on the B737-800 [11]	12
2	Most common vortex generators (John C. Lin [9])	13
3	Results of the different type vortex generators used (John C. Lin [9])	13
4	Baseline (without any vortex generators) (John C. Lin [9])	14
5	Conventional vortex generators (John C. Lin [9])	14
6	sub-scale vortex generator (John C. Lin [9])	15
7	Pressure distributions of the conventional vortex generators (John C. Lin [9])	15
8	Pressure distributions of the sub-scale vortex generators (John C. Lin [9])	16
9	Pressure contours of 2 vortex generators (Neil Titchener et al. [16])	16
10	Lift of the NACA0012 for different mini-tabs heights and chord-length placements of the mini-tabs (Heathcote et al. [4])	18
11	Conceptual design of an active switchable vortex generator: (A) Mini-tab configuration in cruise conditions; (B) Vortex generator configuration in high-lift configuration; (C) Off-state to minimize impact on flow around aircraft [10]	18
12	Universal velocity profile [1]	26
13	Cell skewness	28
14	Cell non-orthogonality	28
15	Cell Aspect ratio	28
16	Workflow of the simulations in 2D	30
17	Computational domain of 2D case around wing	30
18	Mesh of the clean Wing	31
19	Mesh of the wing with the tab	31
20	Mesh around the tab	31
21	Mesh convergence study for 2D case of clean wing	32
22	Result turbulence models	33
23	Pressure coefficient plot comparison for clean wing with $\alpha = 0$ deg, $V_\infty = 20$ m/s	34
24	Lift coefficient for different chordwise placement of mini-tab	35

25	Lift coefficients for varying angle of attack and different chordwise placement of mini-tab. The dotted line is the lift coefficient of the clean wing as reference	35
26	The gradient of the lift coefficient for different chordwise placement of mini-tab	36
27	Pressure coefficient for different chordwise placement of mini-tab	37
28	Velocity contour for different chordwise placement of mini-tab	37
29	Streamlines for different chordwise placement of mini-tab	38
30	Contour plot of the lift coefficient with varying angle of attack and different x^*/c	38
31	Wing planform of the DLR-F25 high-aspect-ratio wing	40
32	Fluid domain	40
33	Surface mesh wing	41
34	Mesh of 3D wing	42
35	Mesh at trailing edge	42
36	Mesh dependency study for $\alpha = 0.6deg$	43
37	Lift coefficient for various angles of attack and turbulence models are compared to CIRA ²	44
38	Lift coefficient vs drag coefficient for different turbulence models compared to CIRA	44
39	Pressure coefficient comparison between NLR and simulation with turbulence $k-\omega$ standard model with $y/b = 0.62$, for $M_\infty = 0.78$ and $\alpha = 2$ degrees	45
40	Pressure coefficient along the chord with $y/b = 0.62$, for $M_\infty = 0.78$ and $\alpha = 0.6$ degrees	46
41	Friction coefficient along the chord of upper surface with $y/b = 0.62$, for $M_\infty = 0.78$ and $\alpha = 0.6$ degrees	46
42	Velocity contour with $y/b = 0.62$, for $M_\infty = 0.78$ and $\alpha = 0.6$ degrees	47
43	Flowchart for the simulations of the mini-tabs	49
44	Sectional lift and drag coefficient for different H/c and AR	50
45	Pressure coefficient along the chord with $y/b = 0.625$, with $AR = 1$, $M_\infty = 0.78$ and $\alpha = 0.6$ degrees with varying H/c	51
46	Velocity contour with $y/b = 0.625$, with $AR = 1$, $M_\infty = 0.78$ and $\alpha = 0.6$ degrees with varying H/c	51
47	Friction coefficient along the chord of upper surface with $y/b = 0.625$, with $AR = 1$, $M_\infty = 0.78$ and $\alpha = 0.6$ degrees with varying H/c	52
48	Streamlines with $y/b = 0.625$, with $AR = 1$, $M_\infty = 0.78$ and $\alpha = 0.6$ degrees with varying H/c	52
49	Pressure coefficient along the chord with $y/b = 0.625$, with $AR = 5$, $M_\infty = 0.78$ and $\alpha = 0.6$ degrees with varying H/c	53
50	Velocity contour with $y/b = 0.625$, with $AR = 5$, $M_\infty = 0.78$ and $\alpha = 0.6$ degrees with varying H/c	54
51	Friction coefficient along the chord of upper surface with $y/b = 0.625$, with $AR = 5$, $M_\infty = 0.78$ and $\alpha = 0.6$ degrees with varying H/c	54
52	Streamlines with $y/b = 0.625$, with $AR = 5$, $M_\infty = 0.78$ and $\alpha = 0.6$ degrees with varying H/c	55

53	Pressure coefficient along the chord with $y/b = 0.625$, with $AR = 7$, $M_\infty = 0.78$ and $\alpha = 0.6$ degrees with varying H/c	56
54	Velocity contour with $y/b = 0.625$, with $AR = 7$, $M_\infty = 0.78$ and $\alpha = 0.6$ degrees with varying H/c	56
55	Friction coefficient along the chord of upper surface with $y/b = 0.625$, with $AR = 7$, $M_\infty = 0.78$ and $\alpha = 0.6$ degrees with varying H/c	57
56	Streamlines with $y/b = 0.625$, with $AR = 7$, $M_\infty = 0.78$ and $\alpha = 0.6$ degrees with varying H/c	57
57	Pressure coefficient along the chord with $y/b = 0.62$, with $AR = 4$, $H/c = 0.015$, for $M_\infty = 0.78$ and $\alpha = 0.6$ degrees	58
58	Velocity contour with $y/b = 0.625$, with $AR = 4$, $H/c = 0.015$, for $M_\infty = 0.78$ and $\alpha = 0.6$ degrees	58
59	Friction coefficient along the chord of upper surface with $y/b = 0.62$, with $AR = 4$, $H/c = 0.015$, for $M_\infty = 0.78$ and $\alpha = 0.6$ degrees	59
60	Lift and drag section coefficients results for different spanwise positions	59
61	Pressure coefficient along the chord at different spanwise distance for $M_\infty = 0.78$ and $\alpha = 0.6$ degrees	60
62	Velocity contour at different spanwise distance for $M_\infty = 0.78$ and $\alpha = 0.6$ degrees	60
63	Friction coefficient along the chord of upper surface at different spanwise distance for $M_\infty = 0.78$ and $\alpha = 0.6$ degrees	61
64	Pressure coefficient along the chord of upper surface at different spanwise positions and $H/c = 0.03$, $AR = 4$ and $x^*/c = 0.15$	62
65	Friction coefficient along the chord of upper surface at different spanwise positions and $H/c = 0.03$, $AR = 4$ and $x^*/c = 0.15$	63
66	Definition of different orientations of the mini-tab	64
67	Lift coefficient for different Wall ratio's and AR with $\theta = 0^\circ$	65
68	Surface pressure drag with $\theta = 0^\circ$ and AR = 10	66
69	Lift coefficient for varying Wall ratio's and AR with $\theta = 25.6^\circ$	66
70	Surface pressure drag with $\theta = 25.6^\circ$ and AR = 10	67

Nomenclature

α	Angle of Attack	C_p	Pressure coefficient
δ_{ij}	Kronecker Delta	$CD * l$	Drag Section Coefficient
ϵ	turbulent Dissipation Rate	CD	Drag coefficient
γ	Heat Capacity Ratio	$CL * l$	Lift Section Coefficient
Λ	Sweep Angle	CL	Lift Coefficient
μ	Dynamic viscosity	H	Height of mini-tab
ν_T	Eddy Turbulent Viscosity	k	Turbulent Kinetic Energy
ω	specific rate of dissipation	M	Mach number
ρ	Density	Re	Reynolds number
τ	Reynolds Stress Tensor	S	strain Tensor
τ_w	Wall Shear Stress	t	Time
θ	Orientation of mini-tabs	u	Velocity
AOA	Angle Of Attack	u_τ	frictional Velocity
AR	Aspect ratio of mini-tab	V	Velocity
b	Wingspan	x	x coordinate along the chord line
c	Chord Length	x^*	Placement of mini-tab along the chord-line
C_{fx}	Skin friction coefficient	y	y coordinate along the wing span
$C_{p,crit}$	critical pressure coefficient	y^+	Non-dimensional wall distance

2

Introduction

2.1. Relevance of the Project

Aircrafts experience a variety of aerodynamic loads during their flight operation. These aerodynamic loads can range from impulsive loads to maneuvers that the aircraft needs to perform. These loads can add considerable stress on the aircraft increasing the risks of deformation and fatigue failure. To mitigate these loads multiple techniques are used. These load alleviation techniques are used to reduce not only the magnitude of the loads but also the fluctuations of the loads [12].

The current load alleviation techniques that are used on aircrafts are mostly passive devices [15]. These devices reduce the load by inducing wash-out and/or by reducing flow separation. These techniques are however as stated passive. The consequence of this is that these devices are often only effective for specific conditions that they are designed for. Active load alleviation techniques are also used ([17]) which utilize the aircraft control surfaces. The downside of using these control surfaces is their limited effectiveness for loads that are defined by high frequencies. This limitation arises due to the considerable inertia and mass of the control surfaces, which makes it difficult to move fast enough to counteract these loads [5, 8].

In recent years a new technique has emerged that uses mechanical devices called mini-tabs. Studies [5] have shown that these small devices can change the lift produced by the wings. These devices are usually mounted at the upper surface of a wing and proved to be effective in reducing the lift. Experimental studies ([4]) have shown that the chord-wise placement of these devices are an important factor in reducing the lift of a wing.

As these studies have shown that these new devices can be very beneficial by reducing the lift and in extension the loads on the wings. It also shows that the effectiveness of these mini-tabs are influenced greatly by the geometrical factors of the mini-tabs. To optimize these mini-tabs the shape needs to be carefully studied. In this thesis, various geometric factors of the mini-tabs, such as height, aspect ratio, chordwise position, and spanwise position will be varied to investigate the performance of the mini-tab.

2.2. State of the art aerodynamic control systems

As explained in the introduction aircraft encounter a variety of high aerodynamic loads. These high loads can occur for example because of turbulent wind forces and when an aircraft manoeuvres. While these aerodynamic loads are not typical they do dictate often the structural design of an airplane and in extent the weight of the aircraft. Current strategies to mitigate these higher loads are used with the ailerons and flaps of the aircraft and are only used in high speed and low angle of attack. They are not used in high-lift configurations.

In this chapter, various control devices such as mini-tabs, vortex generators, ailerons, flaps and gurney flaps will be discussed and examined to understand their impact on aircraft performance. While the focus of this thesis is on the mini-tabs and their impact on the lift and drag coefficient, understanding how different devices change the aerodynamic properties around an aircraft may provide valuable insight.

2.2.1 Flaps and ailerons

Currently, to mitigate aerodynamic loads, aircrafts rely on flaps and ailerons. These devices alter the wing's lift distribution to reduce aerodynamic loads. However, a significant drawback is their large size, weight, and high inertia. When it comes to countering high-frequency loads, moving the ailerons and flaps quickly becomes challenging [5, 8].

Recent advancements have produced faster and stronger actuators capable of quicker responses ([3]). Nonetheless, this comes with a trade-off: it often necessitates advanced sensors and new control algorithms to maintain aircraft stability. These additional requirements contribute to increased weight and complexity, ultimately diminishing the overall effectiveness of this technique.

2.2.2 Vortex generators

Another technique employed that changes the aerodynamics around a wing is the use of vortex generators. A boundary layer loses energy because of the friction inside the fluid. This loss in energy can lead to flow separation which is not preferred. A vortex generator utilizes the free stream fluid above the boundary layer to delay flow separation by creating vortices that energize the slow-moving boundary layer. As a result, the flow gains more momentum, leading to a delay in flow separation. An example of these devices can be seen in Fig.1:

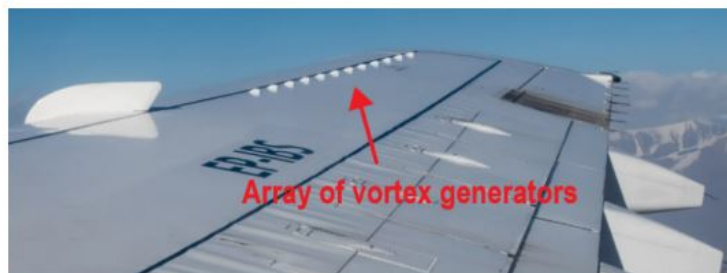


Figure 1: Vortex generators used on the B737-800 [11]

There has been some extensive research on vortex generators. One of them is from John C. Lin [9]. This article shows the results of different vortex generator designs and their effectiveness in reducing the separation region. Some of the devices that are tested are the counter-rotating, co-rotating, wishbone and doublet devices (Fig. 2). The way that these systems create vortices differs but the underlying reason is the same. To create strong vortices to delay flow separation by creating a high-pressure and low-pressure region. The effectiveness of these vortex generators was compared against each other by observing how much the vortex generators reduced the separated region.

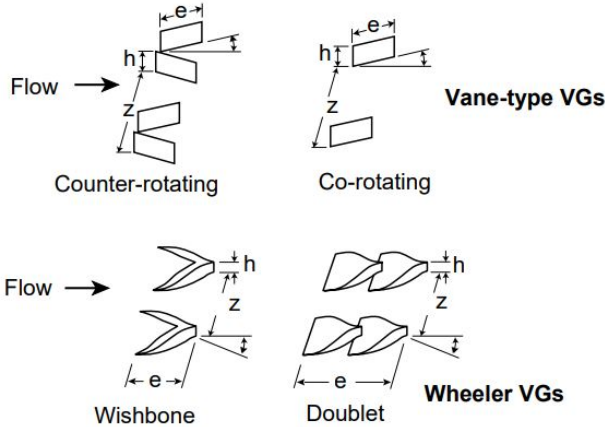


Figure 2: Most common vortex generators (John C. Lin [9])

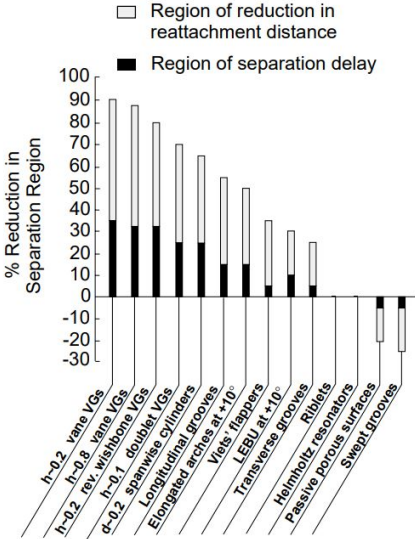


Figure 3: Results of the different type vortex generators used (John C. Lin [9])

The results indicate that vane-type vortex generators are more effective in delaying flow separation than any other vortex generator, while also producing lower drag. It also demonstrates that the smaller sub-scale vane-type vortex generator is more efficient than the conventional vane-type vortex generator in reducing the separated region. This can shift the

focus of newly designed vortex generators towards vane-type sub-scale vortex generators since these are the most effective ones.

2.2.3 Conventional and sub-scale vortex generators

The most effective vortex generators are the vane-type ones. There are however two different kinds of vane-type generators namely conventional with a height of 0.8 - 1.5 times the boundary layer and sub-scale vortex generators with a height of typically just 20 % of the boundary layer. These devices are completely "submerged" in the boundary layer. From Fig.3 it can be observed that these small devices have the same effectiveness as the conventional ones. The reason behind this observation is that in the 20 % of the boundary layer thickness the velocity is equal to around 80 % of the free-stream velocity. The vortices created will be because of this phenomenon equal to the conventional vortex generator. This shows that a larger vortex generator may not be beneficial as this will create higher drag and also introduce more 3D effects. This is shown in figures 4 to 6.

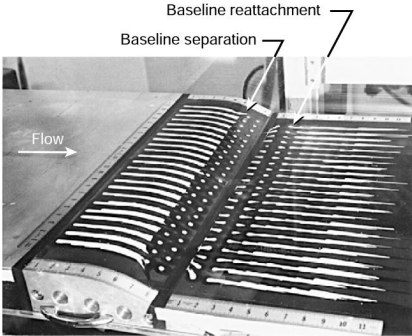


Figure 4: Baseline (without any vortex generators) (John C. Lin [9])

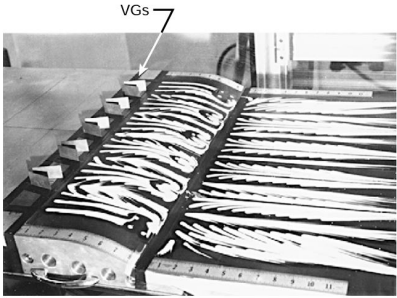


Figure 5: Conventional vortex generators (John C. Lin [9])

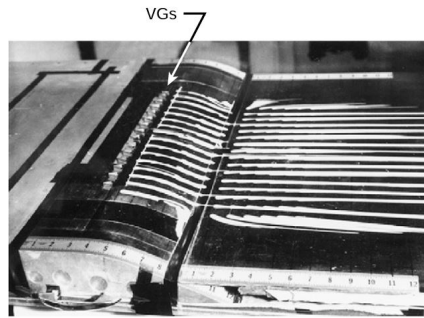


Figure 6: sub-scale vortex generator (John C. Lin [9])

Figure 4 shows the experiment without any vortex generators. The separation line and reattachment can be observed from this figure. Fig. 5 shows the results after using the conventional vortex generators. The separated region is indeed strongly reduced but some strong 3d effects can be observed. This is probably because the vortex generators also create a strong re-circulation zone. This indicates that the vortices created may be too strong.

Figure 6 shows the result from the sub-scale vortex generators. It can be seen that not only is the separated region reduced when compared to the baseline without any vortex generators but there are also no re-circulation zones present by creating too strong vortices. This shows that these devices perform better when compared to the conventional ones.

To demonstrate the 3d effects multiple pressure distribution slices are made at a certain spanwise distance from the middle of the vortex generators. The results can be seen in figures 7 and 8:

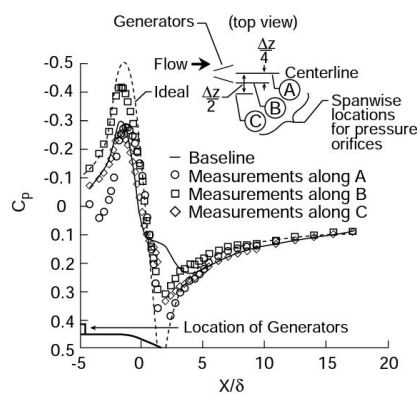


Figure 7: Pressure distributions of the conventional vortex generators (John C. Lin [9])

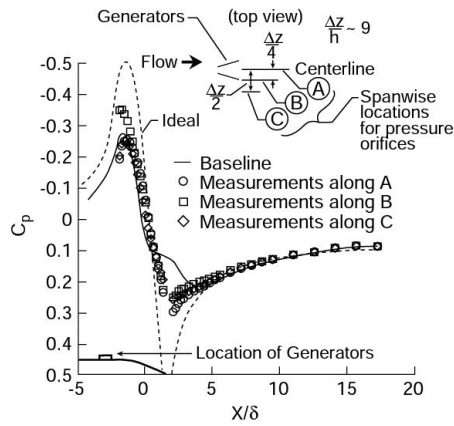


Figure 8: Pressure distributions of the sub-scale vortex generators (John C. Lin [9])

Figure 7 shows the pressure distributions of the conventional vortex generator. A, B and C are slices with a different span-wise position. It shows that the flow recovers to the ideal case much quicker when compared to the baseline but it also shows the differences in pressure at these 3 slices. This shows that these devices create strong 3D effects and the vortices created may be too strong.

Figure 8 shows the pressure distributions of the sub-scale vortex generator. The pressure distributions are closer to each other at the different slices which explains the difference with the conventional device. It shows that the sub-scale devices create little to no 3D effects while still recovering much quicker to the ideal case.

A study from Neil Titchener et al. ([16]) shows that an important parameter for designing an vortex generator is the distance between the vortex generators. If the distance is too small the vortices created by the devices may interact with each other negatively. This is shown in Fig. 9. It shows the pressure contours and the vortices created by the vortex generators. It indicates that when the vortex generators are too close to each other the counter-rotating vortices will cancel each other out mostly. It is also suggested that the height of the vortex generator determines mostly how strong the vortices are and in extent the spacing between the devices.

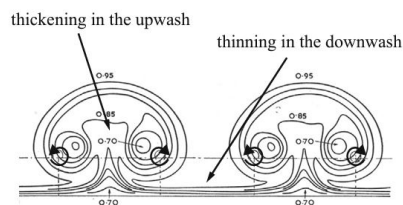


Figure 9: Pressure contours of 2 vortex generators (Neil Titchener et al. [16])

The problem with these devices is that because they are passive they only work for specific flight conditions that they are designed for and may even impact the flow negatively outside these flight conditions. A new technique needs to be developed to make these vortex generators active, enhancing their effectiveness across a wider range of an aircraft's flight conditions.

2.2.4 Gurney flap

A device that is also used to change the lift generated by the wings are Gurney flaps ([19]). These flaps are usually put at the lower side of a wing. This device works by creating a pair of counter-rotating vortices behind it. This will displace the Kutta condition and accelerate the flow at the upper side of the wing. While this increases the lift produced by the wing, it also results in increased drag and often adds weight, leading to lower performance.

2.2.5 Mini-tab

The main techniques that are used nowadays are the use of flaps and ailerons, vortex generators and Gurney flaps. The question now arises if there is a device that is small and lightweight so that it can work with high-frequency changes, can be put on a wing without too much difficulty and can be made active so that it will work in different flight regimes and conditions. From this question, new researches have begun in the last few years into mini-tabs. These mechanical devices work like the Gurney flap in the sense that they create a vortex behind it to change the lift distribution. The difference is that the mini-tabs are placed at the upper side of the wing.

Insights into the design of mini-tabs have been gained through research. The research from Heathcote et al. [4] performed experiments on a NACA 0012 airfoil with mini-tabs. They researched what effect the chord-wise placement of the mini-tabs and length of the mini-tabs have on the lift reduction. This not only provides a valuable starting point in validating the obtained results but also gives some insights into how these geometrical factors change the flow of the airfoil. A few things can be observed from the experiments.

The first thing that can be observed from figure ?? is the further the mini-tab is placed from the leading edge the higher the lift reduction. The second thing that can be seen from the results is that for the mini-tab with a height of 4% of the chord length, the maximum lift reduction is when the mini-tab is placed at around 60% of the chord length.

The results also show that the lift reduction is fairly linear when compared to the angle of attack. For the mini-tab with a height of 2% of the chord length, the lift reduction reduces almost linear for low angle of attacks. For the mini-tabs with height 4% of the chord length it actually shows that when the mini-tabs are placed at 60% of the chord length or more the lift increases almost linear even for high angle of attacks. This is beneficial when designing the mini-tabs. Because of this linearity, it would be easier to predict the lift reduction when designing the control algorithms of the mini-tabs.

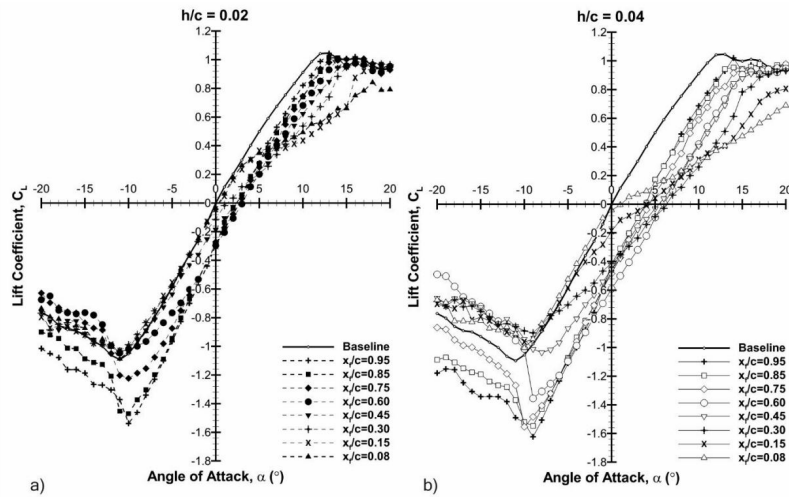


Figure 10: Lift of the NACA0012 for different mini-tabs heights and chord-length placements of the mini-tabs (Heathcote et al. [4])

2.3. Research Question(s)

A new active device is theorized that combines the vortex generator and mini-tab. This device is called an **Active Switchable Vortex Generator (ASVG)**. A novel conceptual design is made and illustrated in Fig.11. An **ASVG** can switch between functioning as a vortex generator to delay flow separation during low-speed, high-angle-of-attack flight regimes, and as a mini-tab to induce flow separation for reducing the lift coefficient during high-speed, low-angle-of-attack flight regimes when required. It has also the ability to be switched off to reduce its impact on the lift distribution and reduce the drag it develops. This is simply done by aligning the device with the main airflow. To work like a spoiler/mini-tab the device needs to be rotated 90° (figure 11A) with respect to the main flow and to work like a vortex generator the ASVG needs to be rotated between 0° and 90° (figure 11B). A device as such can be switched quickly to mitigate any high-frequency loads and work in a variety of flight conditions.

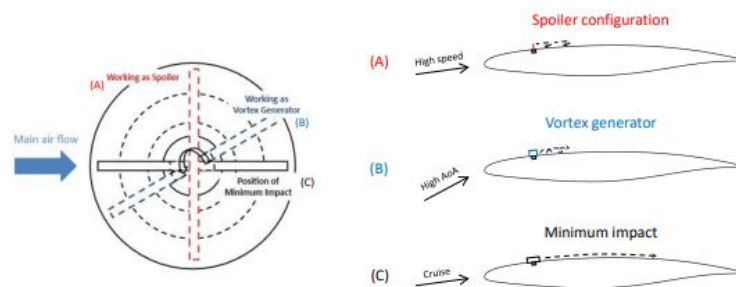


Figure 11: Conceptual design of an active switchable vortex generator: (A) Mini-tab configuration in cruise conditions; (B) Vortex generator configuration in high-lift configuration; (C) Off-state to minimize impact on flow around aircraft [10]

To pave the way into the designing of the ASVG, this thesis will begin with the first step: the mini-tab. This will deepen the understanding of the workings of a mini-tab and lay the

foundation for future research into the ASVG's. Most literature found on mini-tabs are often performed under simplifying assumptions, such as low-speed flight regimes. There is some experimental work done on 3D cases but not on full-scale aircraft wings. This leaves a prominent research gap that creates a need for a more comprehensive research

Because of this, the thesis consists of the following **main research question**:

- 1.** The first research question is how the geometrical factors change the effectiveness of the mini-tab in high speed and low angle of attack flight regime by performing CFD analysis
 - (a)** What are the key performance metrics or parameters to assess the effectiveness of mini-tab in these flight conditions and how do they vary with different geometrical configurations
 - (b)** How do changes in the mini-tab's geometrical factors influence the flow characteristics and aerodynamic behavior of the aircraft?

Theoretical Framework of Computational Fluid Dynamics

In this chapter, the underlying equations governing fluid motion and key mesh criteria will be discussed next. The discussion begins with what is called the closure problem. Before going into this, it is however necessary to understand the Navier-Stokes equations which describe the motion of fluids.

3.1. RANS equations and closure problem

Equation 1 is the continuity equation and Eq. 2 is the momentum equation. Solving these equations directly (e.g. by DNS) however, would demand a significant allocation of computational resources. Multiple solutions are available for this problem. A common solution is the Reynolds-Averaged-Navier-Stokes model. This solution solves the Navier-Stokes equation by recognizing that the flow variables can be split into two parts. The first part is the average of the flow variable and the second one is the fluctuating part around the average. This is also called the Reynolds decomposition. The next equations will demonstrate how this is implemented.

$$\frac{\partial \rho}{\partial t} + \nabla(\rho \vec{u}) = 0 \quad (1)$$

$$\frac{\partial \rho \vec{u}}{\partial t} + \nabla(\rho \vec{u} \vec{u}) + \nabla p = \rho \vec{f} + \nabla \tau \quad (2)$$

First, the velocity is split into two parts as discussed previously:

$$u_i(x, t) = \bar{u}(x) + u'(x, t) \quad (3)$$

$$\bar{u}(x) = \frac{1}{T} \int_t^{t+T} u(x, t) dt \quad (4)$$

The term $\bar{u}(x)$ is the time average of the velocity and $u'(x, t)$ equals the fluctuating part. Equation 5 takes the average of $\bar{u}(x)$ which is equal to itself.

$$\overline{\overline{u}}(x) = \frac{1}{T} \int_t^{t+T} \overline{u}(x) dt = \overline{u} \quad (5)$$

When considering the average of $u'(x, t)$ the integral in Eq. 6 is evaluated. The sum in the integral is obtained from Eq. 3. Looking at the first term of the integral results in $\overline{u}(x)$ and the second term results in $\overline{\overline{u}}(x)$ which from Eq. 5 equals to \overline{u} .

$$\overline{u'}(x, t) = \frac{1}{T} \int_t^{t+T} [u_i(x, t) - \overline{u}(x)] dt = \overline{u}(x) - \overline{\overline{u}}(x) = 0 \quad (6)$$

This way only the average of the flow properties have to be calculated without the need for the fluctuating part. If this is now implemented into Eq. 1 the following expressions are obtained:

$$\frac{\partial(\rho + \rho')}{\partial t} + \nabla(\rho + \rho')(u + u') = 0 \quad (7)$$

$$\frac{\partial \overline{\rho}}{\partial t} + \nabla(\overline{\rho u} + \overline{\rho' u'}) = 0 \quad (8)$$

Equation 8 is obtained when the Reynolds-average is calculated from Eq. 7. After performing the Reynolds averaging, certain terms emerge, for example, $\overline{\rho' u}$. This term however equals zero since the average of the fluctuating parts is zero and has no correlation with the mean flow variables. The last term $\overline{\rho' u'}$ however is not equal to zero since the fluctuating parts of the flow variables are correlated. This opposes a problem because now an additional equation needs to be solved. To solve this problem Eq. 3 needs to be changed. A different kind of averaging needs to be performed. Instead of just time averaging, the equations can also be mass-averaged. This is also called Favre-averaging. This is done in the following way:

$$\tilde{u}(x) = \frac{1}{\overline{\rho}} \frac{1}{T} \int_t^{t+T} \rho(x, t) u(x, t) dt = \frac{\overline{\rho u}}{\overline{\rho}} \quad (9)$$

$$\tilde{u}(x) = \frac{\overline{\rho u}}{\overline{\rho}} \quad (10)$$

$$\overline{\rho} \tilde{u} = \overline{\rho u} \quad (11)$$

$$\overline{\rho} \tilde{u} = \overline{\rho u} + \overline{\rho' u'} \quad (12)$$

Equation 10 is the mass average of the instantaneous velocity. Eq. 12 is obtained by expanding Eq. 11 utilizing the Reynolds decomposition and Reynolds-averaging. When Eq. 12 is put into Eq. 8, the following equations are obtained:

$$\frac{\partial \bar{\rho}}{\partial t} + \nabla((\bar{\rho} \tilde{u} - \overline{\rho' u'}) + \overline{\rho' u'}) = 0 \quad (13)$$

$$\frac{\partial \bar{\rho}}{\partial t} + \nabla(\bar{\rho} \tilde{u}) = 0 \quad (14)$$

Equation 14 is the final equation and by using the Favre-averaging technique the correlation between the fluctuating flow variables is lost and no extra equations are required to solve this equation now.

For the momentum Eq. 2 the same techniques are being used. For convenience, the external force is dropped. When using the Favre-averaging, Reynolds decomposition and Reynolds-averaging the following equation is obtained:

$$\frac{\partial \bar{\rho} \tilde{u}}{\partial t} + \frac{\partial(\bar{\rho} \tilde{u}_i \tilde{u}_j)}{\partial x_j} = -\frac{\partial \bar{p}}{\partial x_i} + \frac{\partial(\bar{\tau}_{ij} - \overline{\rho u''_i u''_j})}{\partial x_j} \quad (15)$$

The variable τ_{ij} is the stress tensor that defines the strain rate at a certain point in the flow. It can be split into two parts where one part is symmetric and the other part asymmetric. The symmetric part is called the strain tensor which calculates the velocity gradients at a certain point in the velocity field. The asymmetric part is called the vorticity tensor.

In equation 15 the term $\overline{\rho u''_i u''_j}$ requires modelling to be solved properly. This is due to the complex correlations of the fluctuating velocity components, represented by u''_i and u''_j . These correlations are difficult to determine directly due to the chaotic and unpredictable nature of turbulent flows. There are multiple ways to solve this turbulence problem. The most common ones are the eddy viscosity models and Reynolds stress models. There exist multiple eddy viscosity models which differ in how many transport equations they use. The most common ones are the Spalart-Allmaras, $k - \epsilon$ and $k - \omega$ models. The similarity between these models is that they all are based on the Boussinesq hypothesis which states that the turbulent stresses are related to the shear stresses and that a turbulent viscosity ν_T connects these terms. The following equations are used:

$$\overline{\rho u''_i u''_j} = 2\nu_T S_{ij} - \frac{2}{3}\delta_{ij}k \quad (16)$$

$$S_{ij} = \frac{1}{2} \left(\frac{\partial \bar{u}_i}{\partial x_j} + \frac{\partial \bar{u}_j}{\partial x_i} \right) \quad (17)$$

$$k = \frac{1}{2} (\overline{u'_i u'_i}) \quad (18)$$

Equation 17 calculates the mean strain tensor, denoted as S_{ij} . The components of the strain tensor are computed by summing the spatial derivative of the mean velocity component \bar{u}_i with respect to x_j and the spatial derivative of the mean velocity component \bar{u}_j with respect to x_i .

Equation 18 defines the turbulent kinetic energy, denoted as k . It is calculated by squaring the fluctuating velocity component u'_i . δ_{ij} is called the Kronecker delta which equals one when $i = j$ and otherwise zero. The final step in this process is to model the eddy turbulent viscosity ν_T . The upcoming chapter will explain how the different models achieve this.

3.2. Different solutions for closure problem

3.2.1 Spalart-Allmaras model

The Spalart-Allmaras (S-A) model solves the eddy viscosity by introducing a transport Eq. 19 [14]. It uses one transport equation and therefore is categorized as a one-equation turbulence model. The Spalart Allmaras is a popular turbulence for a few reasons. The first reason is that less computational power is needed since there is just one turbulence variable to solve. Not only does this reduce the time necessary to solve the simulations but also decreases the amount of memory needed.

There are however some limitations. The first disadvantage is the use of only one turbulence variable. While using one variable utilizes less memory and computational power it does however have difficulty simulating separated flow. It under-predicts flow separation and one should be careful when using this model in such situations. The equation governing the modeling of eddy turbulent viscosity is illustrated by Eq. 19.

$$\frac{\partial \tilde{v}}{\partial t} + u_j \frac{\partial \tilde{v}}{\partial x_j} = c_{b1}(1 - f_{t2})\tilde{S}\tilde{v} - \left[c_{w1}f_w - \frac{c_{b1}}{k^2}f_{t2} \right] \left(\frac{\tilde{v}}{d} \right)^2 + \frac{1}{\sigma} \left[\frac{\partial}{\partial x_j} \left((v + \tilde{v}) \frac{\partial \tilde{v}}{\partial x_j} + c_{b2} \frac{\partial \tilde{v}}{\partial x_i} \frac{\partial \tilde{v}}{\partial x_i} \right) \right] \quad (19)$$

$$\begin{aligned} \nu_T &= \rho \tilde{v} f_{v1} & f_{v1} &= \frac{\chi^3}{\chi^3 + c_{v1}^3} & \chi &= \frac{\tilde{v}}{v} \\ \tilde{S} &= \Omega + \frac{\tilde{v}}{k^2 d^2} f_{v2} & f_{v2} &= 1 - \frac{\chi}{1 + \chi f_{v1}} & f_w &= g \left[\frac{1 + c_{w3}^6}{g^6 + c_{w3}^6} \right]^{\frac{1}{6}} \\ g &= r + c_{w2}(r^6 - r) & r &= \frac{\tilde{v}}{\tilde{S} k^2 d^2} & f_{t2} &= c_{t3} e^{-c_{t4} \chi^2} \end{aligned} \quad (20)$$

Constant	Value
c_{b1}	0.1335
σ	2/3
c_{b2}	0.622
k	0.41
c_{w2}	0.3
c_{w3}	2
c_{v1}	7.1
c_{t3}	1.2
c_{t4}	0.5
c_{w1}	$\frac{c_{b1}}{k^2} + \frac{1+c_{b2}}{\sigma}$

Table 1: Spalart-Allmeras constants

3.2.2 $k - \epsilon$ model

The second model is the $k - \epsilon$ model. It is a 2-equation model meaning that it uses two variables to close the turbulence closure problem. It uses a variable that models the turbulent kinetic energy (k) and a variable that solves the turbulent dissipation rate (ϵ) [6]. It is a reliable model to use for flows that are characterized as free-shear and when there are low-pressure gradients.

Like the S-A model, it has some limitations that should be considered. The most important one is its inaccuracy in modeling the flow if strong adverse pressure gradients are present.

$$\frac{\partial(\rho k)}{\partial t} + \frac{\partial(\rho u_i k)}{\partial x_i} = \frac{\partial}{\partial x_j} \left[\left(\mu + \frac{\mu_t}{\sigma_k} \right) \frac{\partial k}{\partial x_j} \right] + P_k + P_b - \rho \epsilon + S_k \quad (21)$$

$$\frac{\partial(\rho \epsilon)}{\partial t} + \frac{\partial(\rho u_i \epsilon)}{\partial x_i} = \frac{\partial}{\partial x_j} \left[\left(\mu + \frac{\mu_t}{\sigma_\epsilon} \right) \frac{\partial \epsilon}{\partial x_j} \right] + C_1 \frac{\epsilon}{k} (P_k + C_3 P_b) - C_2 \rho \frac{\epsilon^2}{k} + S_\epsilon \quad (22)$$

$$\begin{aligned} \epsilon &= C_\mu^{3/4} \frac{k^{3/2}}{l} & \mu_t &= C_\mu \rho \frac{k^2}{\epsilon} & k &= \frac{3}{2} (ul)^2 \\ l &= \frac{u'}{u} & u' &= \sqrt{\frac{1}{3} (u_x'^2 + u_y'^2 + u_z'^2)} = \sqrt{\frac{2}{3}} k & u &= \sqrt{u_x^2 + u_y^2 + u_z^2} \end{aligned} \quad (23)$$

Constant	Value
C_1	1.44
C_2	1.92
C_μ	0.09
ω_k	1
ω_ϵ	1.3

Table 2: $k - \epsilon$ constants

3.2.3 $k - \omega$ model

The third model is the $k - \omega$ model. It is a versatile and robust model that is widely used in the industry. Like the $k - \epsilon$ model it solves two variables to solve the closure problem [7]. This improves the accuracy but also demands greater memory and computer power. It also resolves the boundary layer adequately even in strong adverse pressure gradients. It does however tend to overpredict the shear flow inside the boundary layer and because of this under-predict flow separation.

$$\frac{\partial(\rho k)}{\partial t} + \frac{\partial(\rho u_j k)}{\partial x_j} = P - \beta^* \rho \omega k + \frac{\partial}{\partial x_j} \left[\left(\mu + \sigma_k \frac{\rho k}{\omega} \right) \frac{\partial k}{\partial x_j} \right] \quad (24)$$

$$\frac{\partial(\rho \omega)}{\partial t} + \frac{\partial(\rho u_j \omega)}{\partial x_j} = \frac{\gamma \omega}{k} P - \beta \rho \omega^2 + \frac{\partial}{\partial x_j} \left[\left(\mu + \sigma_\omega \frac{\rho k}{\omega} \right) \frac{\partial \omega}{\partial x_j} \right] + \frac{\rho \sigma_d}{\omega} \frac{\partial k}{\partial x_j} \frac{\partial \omega}{\partial x_j} \quad (25)$$

$$P = \tau_{ij} \frac{\partial u_i}{\partial x_j} \quad \tau_{ij} = \mu_T \left(\frac{\partial u_i}{\partial x_j} + \frac{\partial u_j}{\partial x_i} - \frac{2}{3} \frac{\partial u_k}{\partial x_k} \delta_{ij} \right) - \frac{2}{3} \rho k \delta_{ij} \quad \mu_T = \frac{\rho k}{\omega} \quad (26)$$

Table 3 are the model constants and Eq. 27 is the auxiliary functions:

Constant	Value
σ_k	0.6
σ_ω	0.5
γ	13/25
C_{lim}	7/8
β	$b_0 f_\beta$
β^*	0.09
β_0	0.0708

Table 3: $k - \omega$ constants

$$f_\beta = \frac{1 + 85\chi_\omega}{1 + 100\chi_\omega} \quad \chi_\omega = \left| \frac{\Omega_{ij} \Omega_{jk} \hat{S}_{ki}}{(\beta^* \omega)^3} \right|$$

$$\hat{S}_{ki} = S_{ki} - \frac{1}{2} \frac{\partial u_m}{\partial x_m} \delta_{ki} \quad \Omega_{ij} = \frac{1}{2} \left(\frac{\partial u_i}{\partial x_j} - \frac{\partial u_j}{\partial x_i} \right) \quad (27)$$

3.2.4 Selection of turbulence model for mini-tab simulation

Experiments from Heathcote et al. [4] showed that the flow behind the mini-tabs is separated. The model that will be used for further simulations needs to accurately and reliably simulate the separated flow. From the properties mentioned for the different models in previous chapters, it becomes clear that the $k - \omega$ model will be the appropriate one to use. It can handle adverse pressure gradients better than the other models and should simulate the anticipated separated flow more accurately.

Nevertheless, all turbulence models will be tested first to ensure the most appropriate model is selected for simulating the separated flow behind the mini-tabs. This will be done for the 2D and 3D case.

3.3. Boundary layer and wall function

The development and resolve of the boundary layer are crucial when performing CFD simulations due to their influence on flow behavior near surfaces. The boundary layer is formed as a result of the no-slip condition that is imposed on solid surfaces. Fluid particles adhere to solid surfaces, where their velocity is zero. This leads to a gradual increase of the velocity when moving further away from a surface. The boundary layer thickness is commonly set to 99 percent of the free stream velocity. This ensures that the velocity gradients and shear forces are captured correctly.

When the flow approaches a surface the velocity gradients increase due to the no-slip condition. This results in higher shear forces and the production of turbulence quantities. However as the velocity of the boundary approaches zero at the surface itself, turbulent flow tends to attenuate, leading to a more stable flow regime.

Because of these interactions inside the boundary layer, a key parameter to resolve the boundary layer correctly is the first cell height. When this cell is too large, important flow properties are not captured accurately and excessively small cell heights may increase the computational power needed to resolve the boundary layer.

To resolve the boundary layer accurately a theory was devised called "The law of the wall" [1]. This principle states that the flow close to a surface is primarily influenced by that same surface, rather than the flow far away from it. An essential component of understanding the Law of the Wall is the universal velocity profile, depicted in Fig.12:

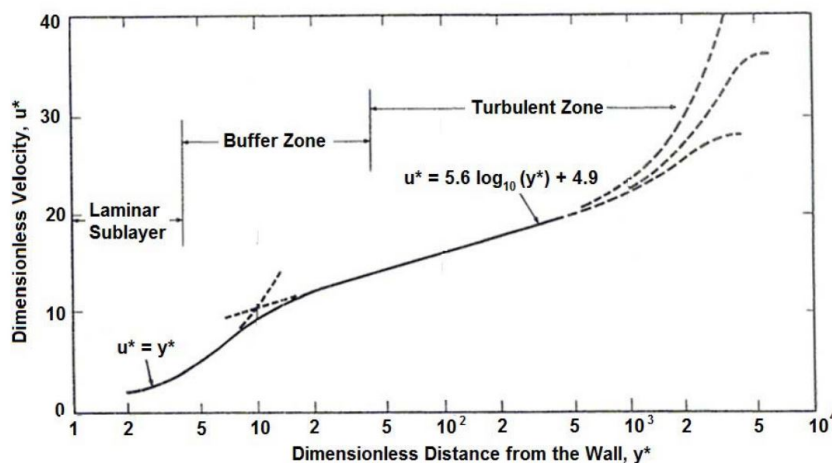


Figure 12: Universal velocity profile [1]

In this profile, the variables y^* and u^* represent the distance from the surface normal-

ized by the viscous length scale and the normalized velocity, respectively. The variables y^* and u^* are calculated using the following equations, derived through dimensional analysis:

$$y^* = \frac{u_\tau \cdot y}{\nu} \quad (28)$$

$$u^* = \frac{U}{u_\tau} \quad (29)$$

where u_τ , known as the frictional velocity, is defined as:

$$u_\tau = \left(\frac{\tau_w}{\rho} \right)^{0.5} \quad (30)$$

where, τ_w represents the wall shear stress, and ρ denotes the fluid density. The frictional velocity relates the shear forces inside the boundary layer to the velocity gradients. It is a key parameter in understanding and characterizing the flow near solid surfaces.

Figure 12 shows that the boundary layer consists of three distinct flow regimes [1]:

- Laminar sublayer: This region is characterized by low velocities close to the wall, which attenuate turbulences in the flow.
- Buffer layer: This flow regime is located between the laminar and turbulent zones. This is where the flow transitions from laminar to turbulent.
- Turbulent zone: The flow in this region is primarily turbulent and leads to increased mixing and momentum exchange in the flow.

Figure 12 also highlights that to resolve the viscous boundary layer accurately y^* should typically be smaller than 5. Higher values of y^* can also be used but instead of resolving the boundary layer, wall functions are used. These are empirical functions that are obtained from experiments and simulations providing an alternative approach to modeling flow near solid surfaces

For this thesis, a y^* value of 1 is chosen. This was done to ensure the accuracy of the simulations.

3.4. Mesh quality criteria

The accuracy and convergence rate of any CFD simulation depends largely on the quality of the mesh. In this study, a conscientious process was involved to ensure the most optimal quality of the generated mesh thereby minimizing its influence on the obtained results. By using a high-quality mesh the accuracy of the simulations was increased and in extent helped the simulations to converge faster. The following 3 mesh qualities were checked for every mesh generated:

- Skewness: The skewness of a cell is measured by comparing the angles of an existing cell with an ideal cell. Fig. 13 shows a perfect hexahedral cell where all the angles are the same whereas for the skewed cell, the angles differ from each other [13].

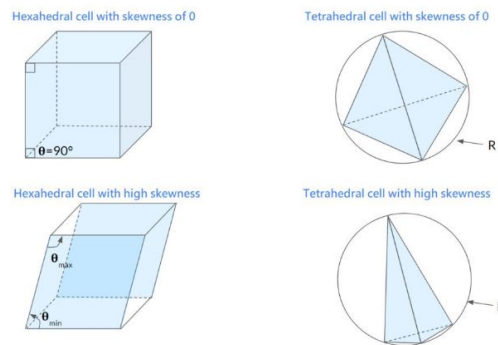


Figure 13: Cell skewness

- Non-orthogonality: Non-orthogonality measures the orthogonality of a face between two cells. When cells show poor non-orthogonal quality that means that the flow between these cells is not aligned with the cells themselves. This will create a numerical instability and as a result, the simulation can take longer to converge or even diverge [13].

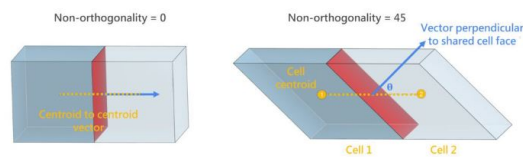


Figure 14: Cell non-orthogonality

- Aspect ratio: Aspect ratio is the ratio between the longest and shortest edge of a cell. High aspect ratio cells can lead to numerical instabilities and decreased accuracy. For example, when the flow has regions of high gradients a high aspect ratio cell will increase the discretization errors because of the limited resolution of the mesh [13].

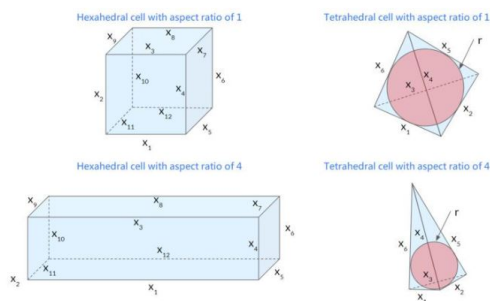


Figure 15: Cell Aspect ratio

Two-dimensional analysis of mini-tab

4.1. Introduction

The objective of these simulations on the 2D case is to understand the intricate aerodynamics of mini-tabs and the tools needed for further simulations. To achieve this the experimentations conducted by Heathcote et al. [4] will be replicated and compared with the obtained results from the simulations. The results from the 2D case will be the groundwork for the 3D case. The next section will explain the methodology to ensure the accuracy of the simulations:

4.2. Methodology

1. Geometry generation

- The first step is to recreate the geometry used in the wind tunnel test. The angle of the wing was made a parameter to change the AOA of the wing.

2. Mesh generation

- After the geometry creation, a mesh was realized. If the initial mesh did not meet predetermined criteria, iterative adjustments were made until a satisfactory mesh was obtained. The criteria that needed to be satisfied were the skewness, aspect ratio and orthogonality of the mesh.

3. Simulation

- The mesh would be used as an input for Ansys Fluent. The calculations were performed with different turbulence models and the most accurate model was chosen. The simulations were then done with this turbulence model until the residuals converged.

4. Mesh convergence study

- To assess the sensitivity of the results to the mesh size, a mesh convergence study was done. This involved using different mesh sizes and evaluating the impact on the simulation outcomes, to establish a mesh-independent solution.

5. Verification with experimental data

- A critical component of the methodology involved verifying the simulation results against experimental data. This step was essential to ensure the accuracy and reliability of the simulations.

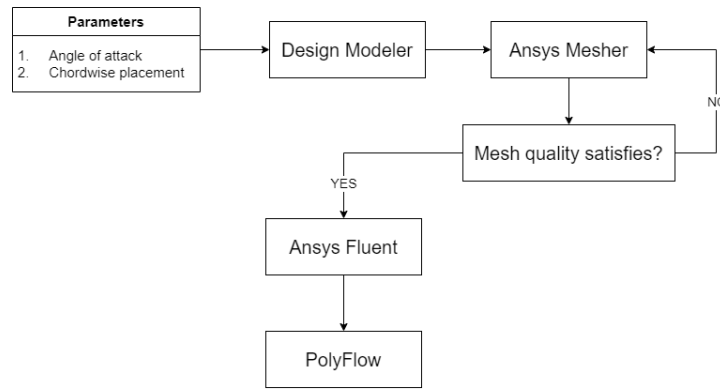


Figure 16: Workflow of the simulations in 2D

Figure 16 shows what the workflow looked like for the clean wing and the wing with the different tabs. The only difference is that the wing with the tab has also the chordwise placement of the tab as a parameter.

4.3. Geometry

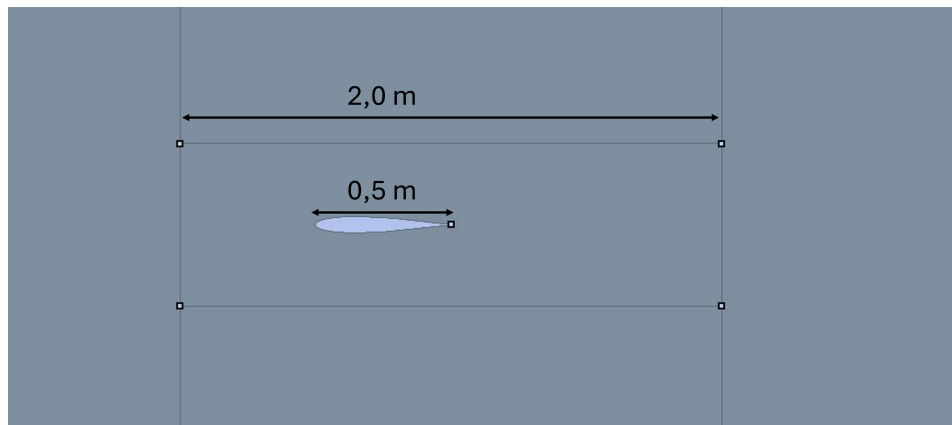


Figure 17: Computational domain of 2D case around wing

The wind tunnel is segmented into multiple sections as in Fig.17. This way a mesh can be made with a fine mesh close to the airfoil and a coarse mesh further away. This will reduce the computational power needed for the simulations. Furthermore, the angle of the airfoil has been parameterized, to automate the geometry generation in the Ansys Workbench environment. Such automation streamlines the simulation process. The length of the computational domain was 20 meters with a height of 2.12 meters to mirror the setup of the experimentation of Heathcote et al. [4].

4.4. Mesh

The success of any CFD simulation depends largely on the quality of the mesh. In this study, a conscientious process was performed to ensure the most optimal quality of the generated mesh. The following images give an example of these meshes.

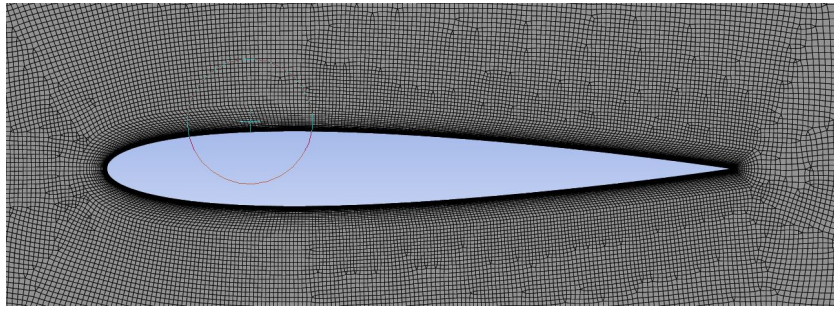


Figure 18: Mesh of the clean Wing

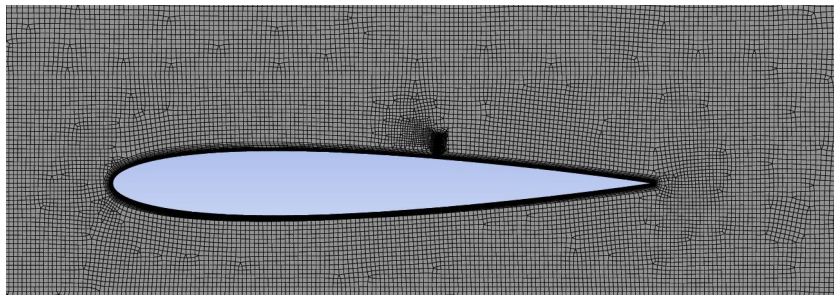


Figure 19: Mesh of the wing with the tab

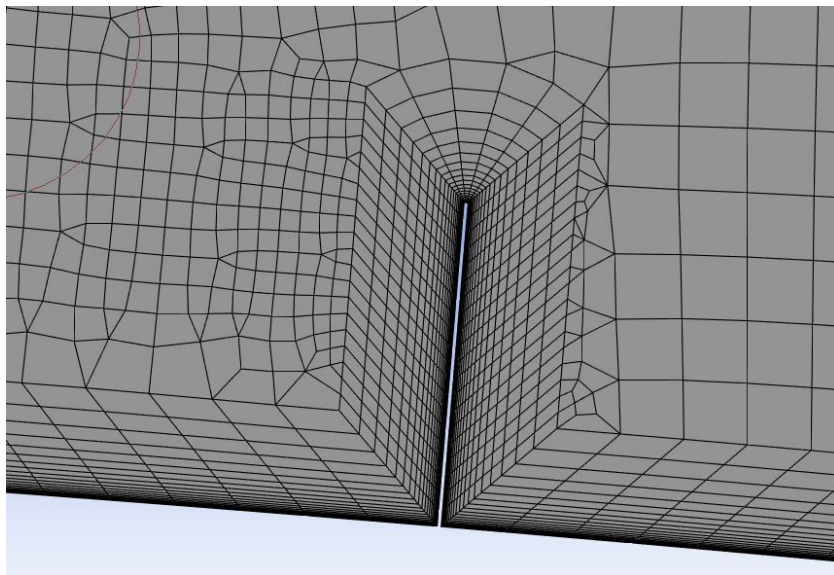


Figure 20: Mesh around the tab

As previously stated an important property of a mesh is the first boundary layer thickness. To capture the boundary layer efficiently a y^+ value of around 1 was obtained. The following equation [18] was used to calculate the first cell height:

$$y_1 = \frac{y^+ \cdot \mu}{\rho \cdot u} \quad (31)$$

The first boundary layer thickness was $1.7 \cdot 10^{-5}$ thick with a total of 30 layers. The following steps were taken to ensure that the quality would be optimal:

- A hybrid mesh, incorporating both quadrilateral and triangular elements, was utilized to effectively capture the geometry. This combination ensures that the mesh accurately represents the complex geometry of the object and also to be memory efficient by the use of quadrilateral elements.
- The wing was designed with curvature consideration to ensure a smooth capture of the leading edge. The minimum degree to capture was set at 1° with a size range between 0.2 mm and 2 mm. This approach ensured an effective capture of the leading edge and in regions with lower curvature, a larger mesh size was employed to reduce the computational power needed for mesh resolution.
- The trailing edge was divided into 20 sections, ensuring that it had a fine enough mesh to capture the flow around the trailing edge effectively.

After the generation of the mesh, the orthogonality, skewness, and aspect ratio were evaluated. If satisfactory the mesh would then be used for the simulations otherwise changes were made.

4.5. Verification

To verify the results that will be obtained by the simulations a couple of things need to be performed and checked first. The first thing that will be done is a mesh convergence study to ensure that the results are not influenced by the quality of the mesh.

4.5.1 Mesh Convergence Study Clean Wing

Figure 21 shows the mesh convergence study. A mesh was made of the clean wing multiple times with an increase in the amount of elements used. This way it could be determined how much the mesh influences the results. The following results were obtained:

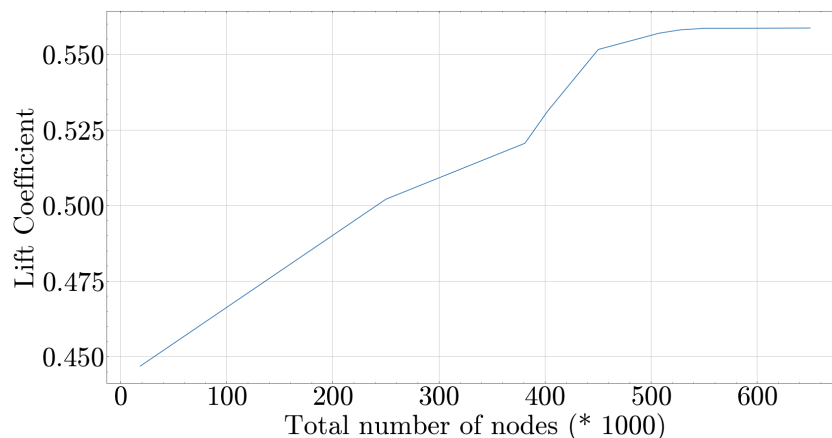


Figure 21: Mesh convergence study for 2D case of clean wing

As can be seen from Fig.21 around $5 \cdot 10^5$ elements the results are converging. For the simulations, a mesh of around $5.5 \cdot 10^5$ elements is used.

4.5.2 Turbulence Model

The next thing is the turbulence model that is going to be used in the simulations. The clean wing is simulated with three different turbulence models namely: Spalart Allmeras, $k-\epsilon$ and $k-\omega$ and compared to the experiment of Heathcote et al. [4]. The ensuing findings reveal the following results:

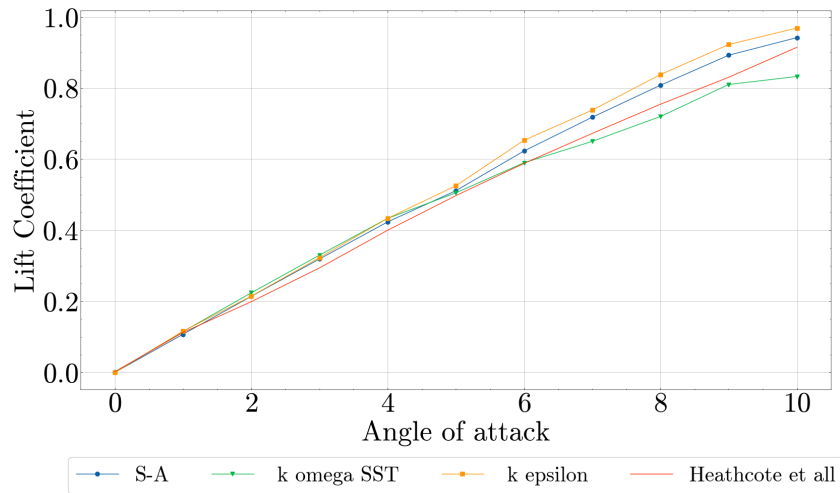


Figure 22: Result turbulence models

Figure 22 shows that the most accurate turbulence model is the Spalart-Allmeras model and this model will be used for further simulations for the 2D case. To ensure that the results of the simulations are accurate the pressure coefficient was also checked in the following section.

4.5.3 Pressure coefficient Clean wing

The clean wing was simulated and the obtained pressure coefficients can be seen in Fig.23. Some differences can be observed. Notably, a disparity was observed between the upper and lower surfaces of the wing in the experimental results. This was not expected since the AOA equals zero and the airfoil is symmetric so that means that the pressure coefficient of the lower and upper surface should be the same.

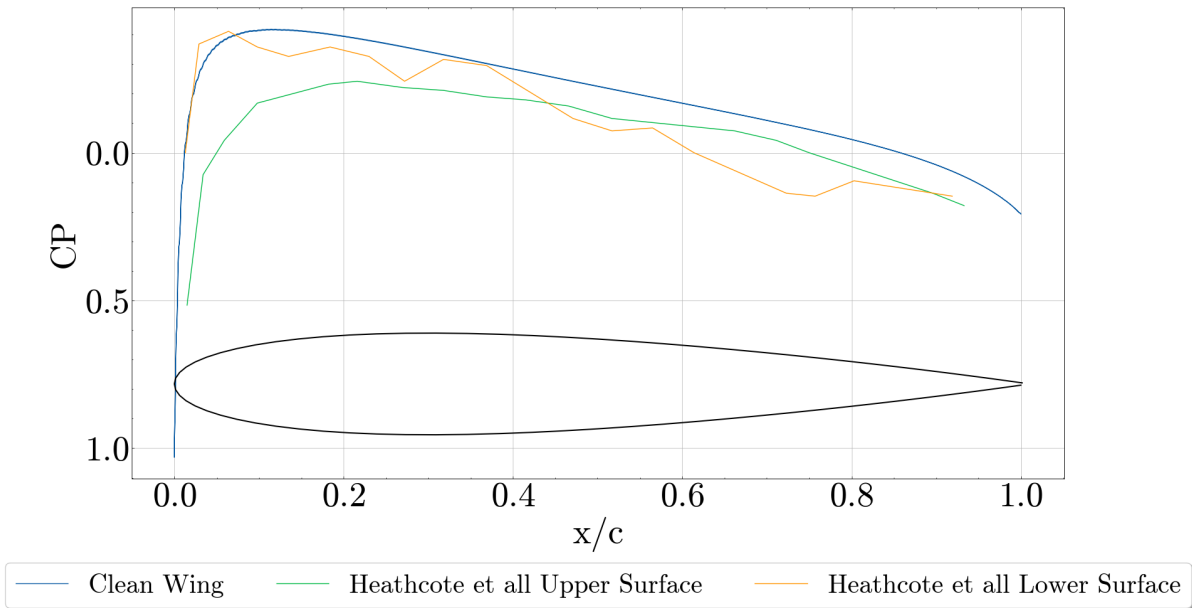


Figure 23: Pressure coefficient plot comparison for clean wing with $\alpha = 0$ deg, $V_\infty = 20$ m/s

This discrepancy is hypothesized to be a consequence of transient effects present during the experiments, a phenomenon not accounted for in the steady-state simulation. The flow was simulated as steady-state and the results show a perfect match for the lower and upper surfaces.

Despite the differences, the overall trend aligns with the experimental results. This indicates that the most important characteristics of the flow were captured.

4.5.4 Lift coefficient comparison between simulation and experiment of mini-tabs

The lift coefficients of multiple mini-tabs at different chordwise positions are compared to the experiments to validate the accuracy of the simulations. Fig.24 shows the comparison between the simulated lift coefficient with varying angles of attack and the experiments from Heathcote et al.[4]. The results from the experiments are indicated with "Ref" and the respective chordwise positions.

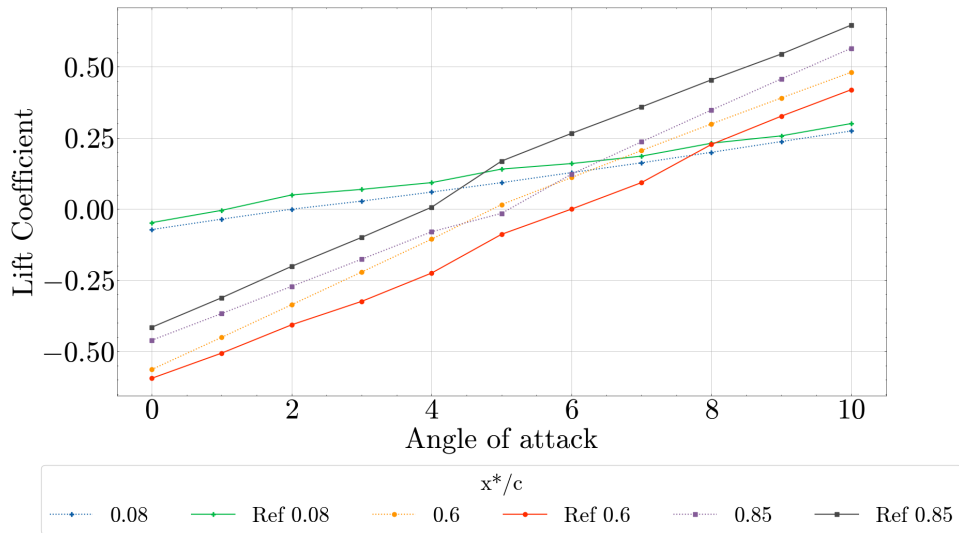


Figure 24: Lift coefficient for different chordwise placement of mini-tab

The simulations exhibit slight differences when compared to the experiments. However, these differences are minor and the overall trend is accurately captured. This shows that the obtained results are accurate and reliable.

4.6. Results

Figure 25 shows the obtained results for changing the chordwise position of the mini-tab with varying angles of attack. From Fig.25 the following key points are observed:

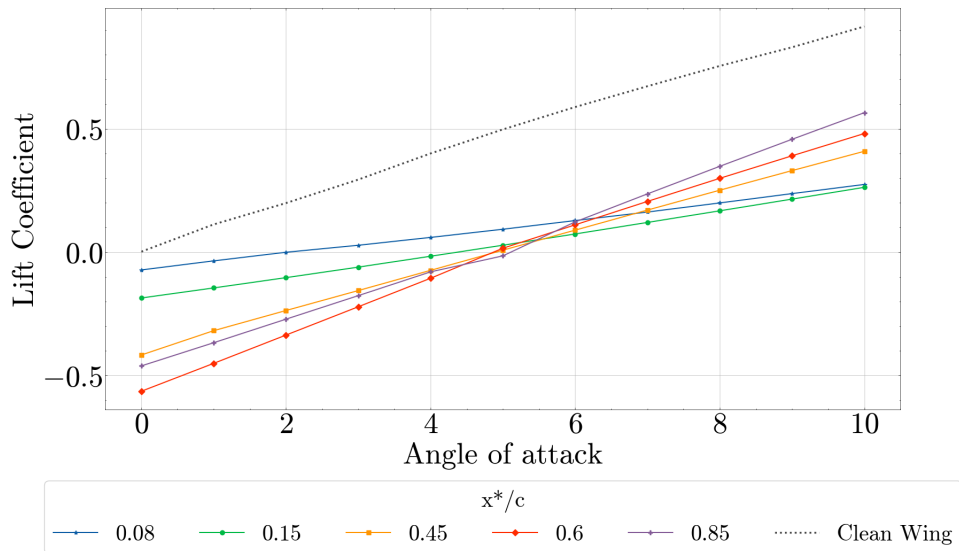


Figure 25: Lift coefficients for varying angle of attack and different chordwise placement of mini-tab. The dotted line is the lift coefficient of the clean wing as reference

Figure 25 illustrates that for low angles of attack, placing the mini-tab closer to the trailing edge (an increase of x^*/c) leads to a reduction of the lift coefficient. However, if the mini-tab is placed after 60 percent of the airfoil chord length, the lift coefficient increases

once more. This increase in lift suggests that placing the mini-tab beyond the 60 percent chord length may negatively impact its performance.

This observation ties in with the effectiveness of mini-tabs at different angles of attack (AOAs). At higher AOAs, mini-tabs placed closer to the trailing edge show a reduction in effectiveness, with the lift coefficients approaching those of the clean airfoil (Fig. 25). This decrease in effectiveness is attributed to the increase of the wake of the airfoil. As the wake expands, mini-tabs that are closer to the trailing edge will be partly or fully immersed and in extent, the effectiveness will be reduced.

The average slope of the lift coefficient lines with respect to the angle of attack in Fig.25 provides more insight into this decrease in the performance of the mini-tab. Mini-tabs that are placed at $x^*/c = 0.6$ show a steeper slope, which indicates that the performance deteriorates faster with an increase of the AOA compared to mini-tabs placed at $x^*/c = 0.08$. This suggests that placing mini-tabs closer to the leading edge may decrease the reduction in lift coefficient but perform better at high angles of attack. Fig.26 shows the gradient of the lift coefficient lines with respect of the placement of the mini-tabs, where a steeper gradient indicates a more significant change in lift coefficient with an increase of the angle of attack. Placing the mini-tab closer to the trailing edge causes steeper lift coefficient lines and greater performance dependence on angle of attack. This additional information supports the relation between the placement and performance of a mini-tab.

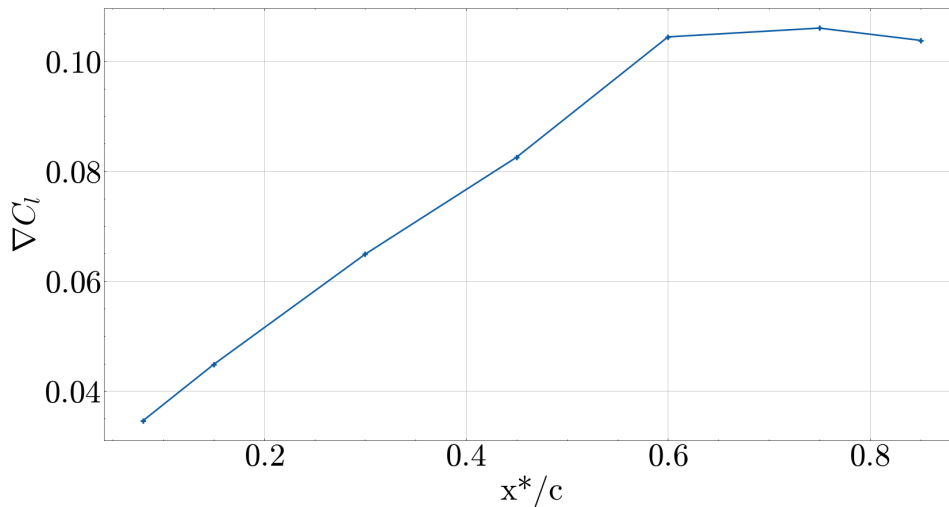


Figure 26: The gradient of the lift coefficient for different chordwise placement of mini-tab

In addition to the CL-AOA relation, one can also investigate the effect of the mini-tab placement on the pressure distribution. Figures 27a and 27b show the pressure distributions for the mini-tab placements at 60 % and 8 % are compared. It is observed that the mini-tab creates a higher pressure at the leading edge when compared the to clean wing. This higher pressure results in a reduction of the lift coefficient. The mini-tab placed at 60 % of the chord length creates a larger region of higher pressure compared to the 8 % placement, suggesting that the decrease in lift coefficient may be more pronounced for the 60 %

placement. This observation aligns with Fig. 25 at low angles of attack. After the mini-tab, a pressure drop can be observed from Fig. 27a. This pressure drop indicates an acceleration in the flow after the mini-tab.

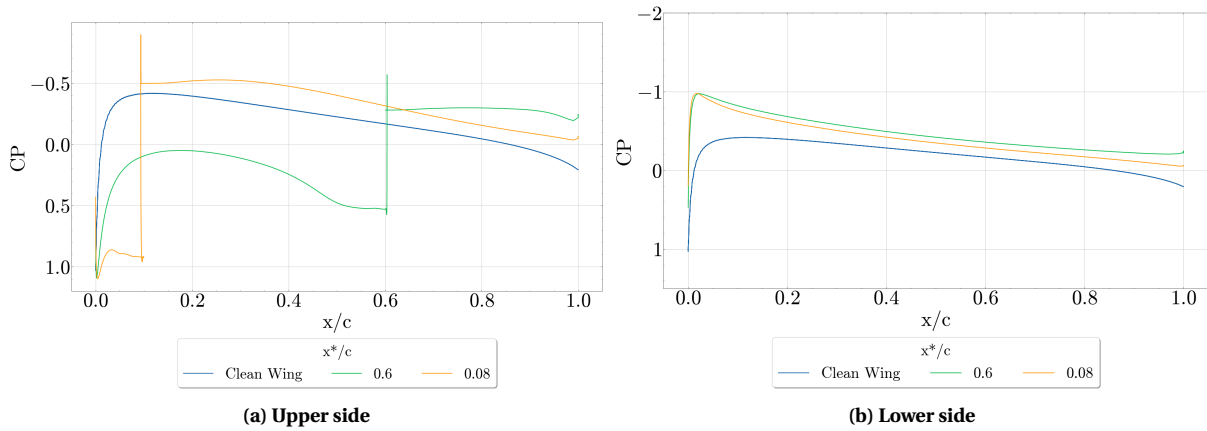


Figure 27: Pressure coefficient for different chordwise placement of mini-tab

A change in the pressure distribution is also observed at the lower surface of the airfoil as depicted in Fig. 27). The pressure coefficient at the lower surface for the 60% case is lower than the 8% case. This disparity arises from the larger high-pressure region created at the leading edge in the 60% case. The resulting apparent change in the angle of attack leads to higher velocity on the lower surface and a reduction of the lift coefficient.

Furthermore, the mini-tab not only changes the pressure distribution at the lower surface but also creates a circulation zone that has an impact on both lift and drag. When the circulation zones of the 60 % case are compared to the 8 % case in Fig. 28 it is observed that for the 8 % case the recirculation zone is bigger than the 60 % case. These recirculation zones are characterized as low-pressure zones. This lower pressure at the upper surface of the airfoil will increase the lift. The expansion of the recirculation zone for the 8% case implies a larger region of lower pressure at the upper surface, leading to an increase in the generated lift. This observation shows a correlation between the size of the recirculation zone and the generated lift.

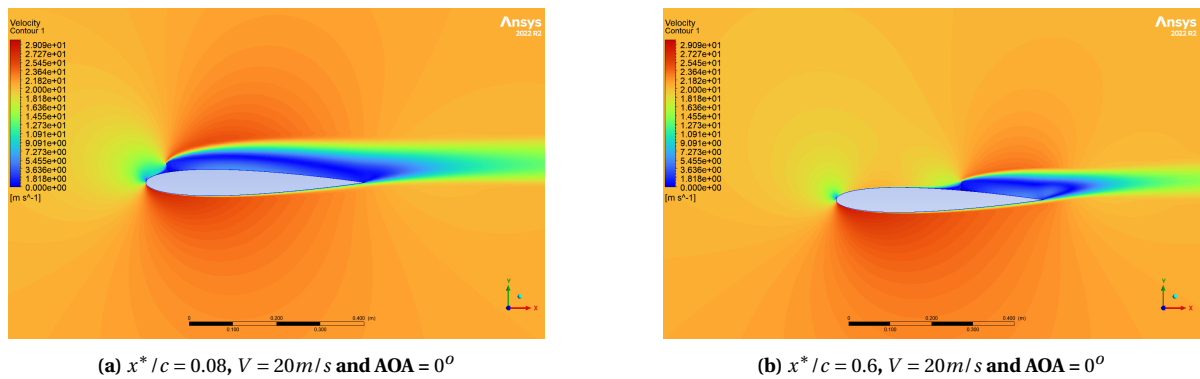


Figure 28: Velocity contour for different chordwise placement of mini-tab

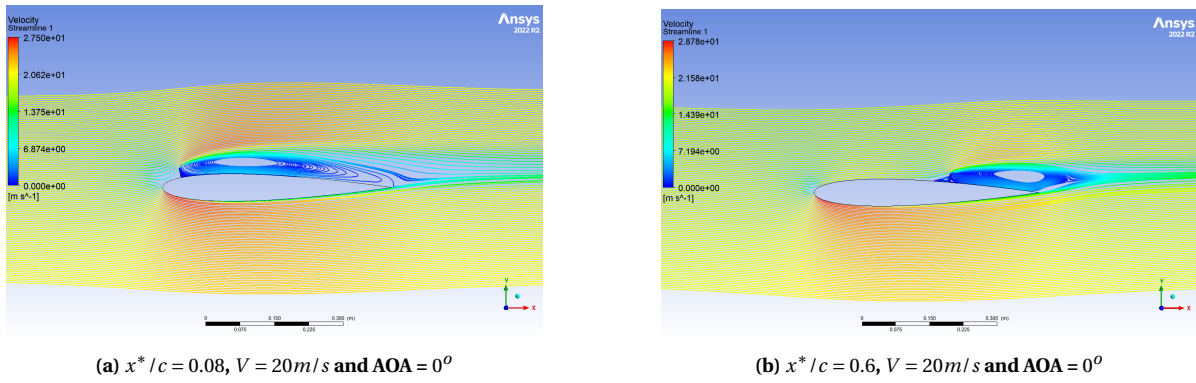


Figure 29: Streamlines for different chordwise placement of mini-tab

4.7. Discussion

A contour plot of the lift coefficient as a function of AOA and mini-tab placement is shown in Fig. 30:

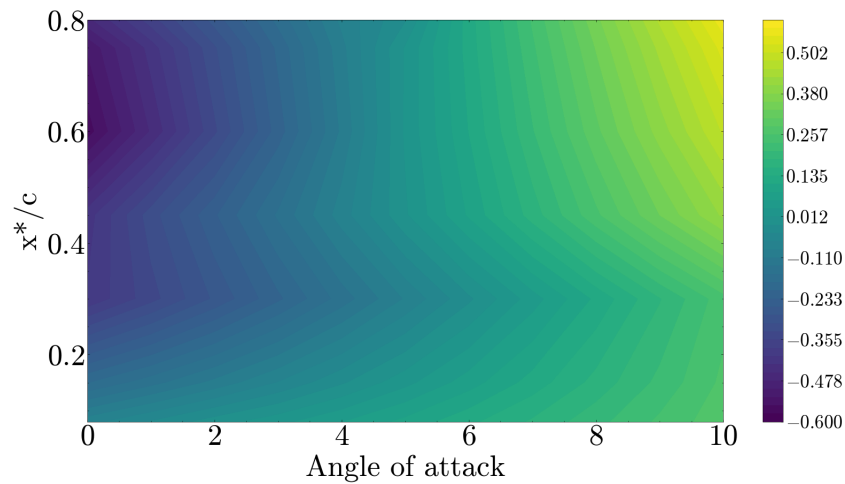


Figure 30: Contour plot of the lift coefficient with varying angle of attack and different x^*/c

The analysis of Fig.30 reveals insightful trends in lift coefficient concerning mini-tab placement and angle of attack. At low AOA, a notable reduction in the lift coefficient is observed until the mini-tab placement exceeds 60 percent of the chord length. This diminishing trend is attributed to the increase in boundary layer thickness, diminishing the effectiveness of the mini-tabs.

Interestingly, at higher AOAs, the efficiency of mini-tab placement at the trailing edge diminishes, as illustrated in Fig. 30. Mini-tabs positioned closer to the leading edge exhibit a lower lift coefficient compared to those near the trailing edge. This suggests that while placing mini-tabs at the leading edge may result in a less pronounced reduction in lift coefficient for low angles of attack, their ability to reduce the lift coefficient at high angles of attack is superior to mini-tabs positioned closer to the trailing edge.

Simulation of clean wing in 3D

5.1. Introduction

In the next step, the 2D study of the mini-tab was extended to a 3D case. This shift from 2D to 3D will introduce additional effects and considerations reflecting a more realistic behavior of the mini-tab on real wings. The transition to 3D simulation will be done with specific objectives:

- In the case of the 2D simulation certain effects were not accounted for in the low-speed regime. In the high-speed regime, an important factor to consider is the compressibility of the fluid. This might create unique shock wave patterns and change the behavior of the fluid around the mini-tab and in extend the performance.
- Realistic behavior: While the results of the 2D case provided us with some important key points on the workings and performance of a mini-tab, it is still simplified. The 2D simulations that were performed in chapter 4 neglected for example spanwise vorticity. Because of these simplifications, a need arises for 3D simulation to provide a more realistic representation of the flow characteristics around mini-tabs on wings. For example, a real wing of an airplane is often swept so this introduces a spanwise flow which was not accounted for in the 2D case.
- Exploration and analysis: There has been limited experimentation conducted with the mini-tabs in 3D high-speed configuration the focus shifts towards exploration and in-depth analysis. The simulations aim to extend the results gained from chapter 4 and uncover the three-dimensional flow patterns and their implications on the lift generated.

As the research progresses into three-dimensional aerodynamics, these objectives will guide the methodology and analyses in the following chapters.

First, the fluid domain and mesh of the wing will be generated. After that, a mesh convergence study will be performed by increasing the amount of elements in the fluid domain. After the mesh convergence study multiple turbulence models will be tested with the DLR-F25 wing, depicted in Fig. 31. A high-aspect-ratio wing which was provided by the DLR. The lift and drag data of the wing were provided and this will be used to compare the turbulence models and select the appropriate one.

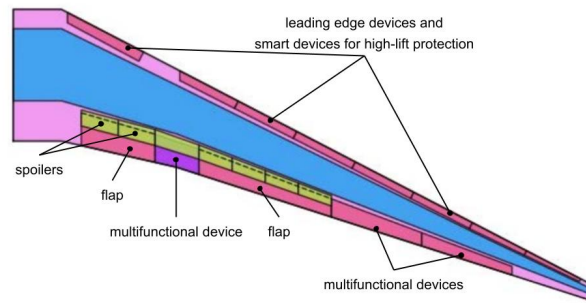
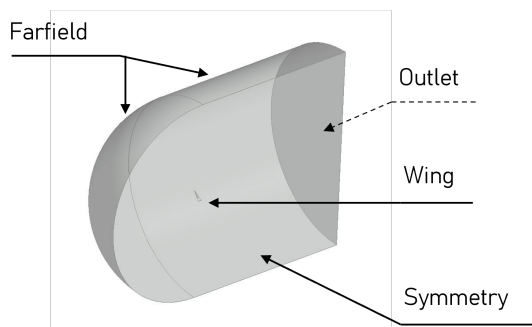


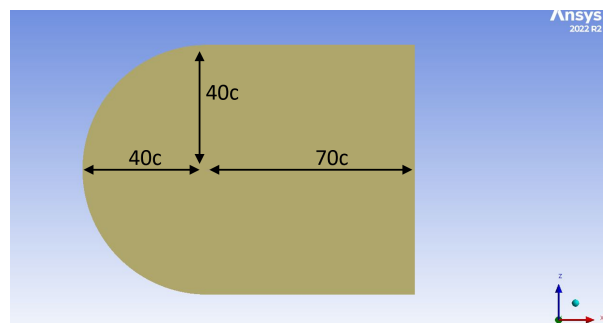
Figure 31: Wing planform of the DLR-F25 high-aspect-ratio wing

5.2. Geometry

A critical aspect of the simulation is the fluid domain. 2 domains are common practice namely a cube and a hemisphere. There are advantages and disadvantages for both. An advantage of using a cube as a computational domain is its simplicity to mesh. A disadvantage however is for a streamlined body like a wing, a cube may require additional elements to capture the shape accurately, increasing the computational power needed. The advantage of using a hemisphere is the curved domain represents the flow pattern around a wing more closely. The complexity of this curved domain is however more complex to mesh than a cube. To capture the flow more accurately the hemisphere was eventually chosen. The fluid domain with the appropriate boundary conditions and dimensions are illustrated in figures 32a and 32b.



(a) Fluid domain boundary conditions



(b) Fluid domain dimensions expressed in wing root chord length

Figure 32: Fluid domain

5.3. Mesh

After defining the fluid domain, the subsequent crucial step involves meshing, a process done through Ansys Fluent Meshing. The program used for this step is Ansys Fluent Meshing. The way that Ansys meshes the fluid domain is done in two steps. The first step is to mesh the surfaces. Multiple options were available namely a triangular or polyhedral mesh. The advantage of a triangular mesh is its simplicity to build a mesh and it often captures

the geometry accurately like the leading edge of the wing. The disadvantage however is that it does not capture the flow accurately and often refinement is needed which increases the computational power. The other option as mentioned is the polyhedral mesh. This type of mesh not only captures the geometry well but also the flow. Because of this, the polyhedral mesh is chosen. Fig.33 illustrates the surface mesh of the wing.

To ensure the quality of the surface mesh the wing was divided into multiple sections. For example the radius of the leading edge at the root is larger when compared to the tip. To capture the fluid around both these regions effectively the elements closer to the tip need to be smaller. This way of dividing the wing will not only ensure the quality of the wing but also decrease the computational power needed.

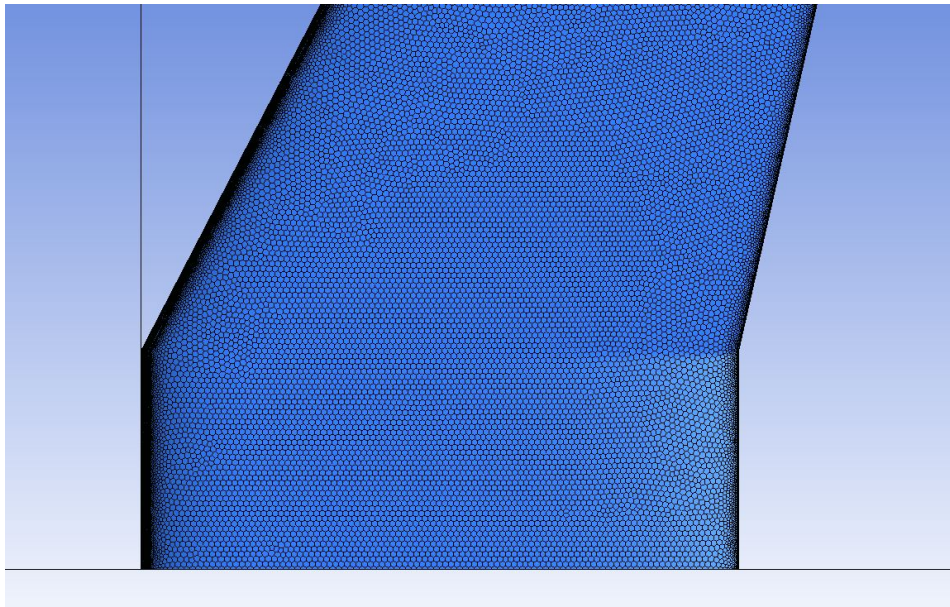


Figure 33: Surface mesh wing

The next step involves meshing the fluid domain. There are several options available for this meshing namely: Polyhedral, Hexcore and Tetrahedral. Tetrahedral elements provide the advantage of accurately capturing the surface contour of the wing. However, using these elements for complex geometries may create elements with poor quality. Another meshing option is the hex-core elements. A hex-core mesh utilizes an octree which is memory efficient, but it may not be able to capture complex geometries accurately, which can again affect simulation accuracy. The third option is to utilize a polyhedral mesh for the computational domain. The benefit of using this element is that it can capture complex geometries accurately. It does however use more nodes per element when compared to the tetrahedral and hex-core which increases the amount of memory needed.

Another volume element that Ansys offers is the Poly-hex mesh. This a hybrid mesh that uses polyhedral and hexcore elements. A polyhedral mesh is created close to the surfaces to ensure that the geometries are captured accurately while far away a hexcore mesh is used to reduce the amount of memory needed. This dual approach harnesses the advantages

of both meshes and thus will not only ensure the quality of the mesh but also decrease the memory needed when compared to the other techniques.

Figures 34 and 35 show the mesh around the wing. In Fig.34 it can be observed that polyhedral elements are used close to the surface and around it a hexcore mesh was utilized. Fig.35 illustrates the trailing edge. As can be seen, the trailing edge was split into multiple elements to capture the wake around the trailing edge effectively. Also, an important feature was the transition from the trailing edge to the upper- and lower side of the wing. This needs to be done smoothly as this can distort the elements and decrease the simulation accuracy. To achieve a high-quality mesh around this transition the surface mesh size of the upper- and lower side of the wing close to the trailing edge was made the same size as the elements on the trailing edge.

The next crucial aspect addressed was the boundary layer. Again like for the 2D case, the first boundary layer thickness was calculated with Eq. 31. The first layer thickness was calculated to be $5 \cdot 10^{-6}$. A total of 30 layers were used.

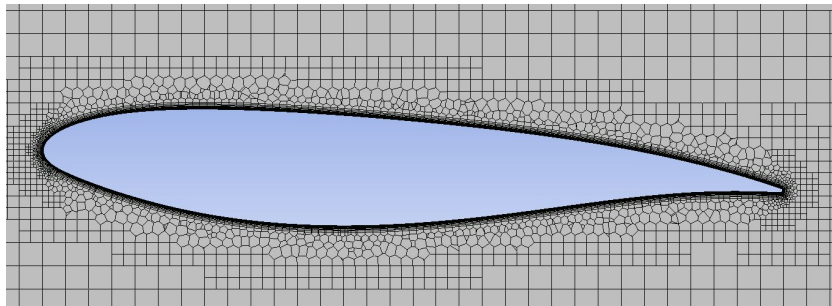


Figure 34: Mesh of 3D wing

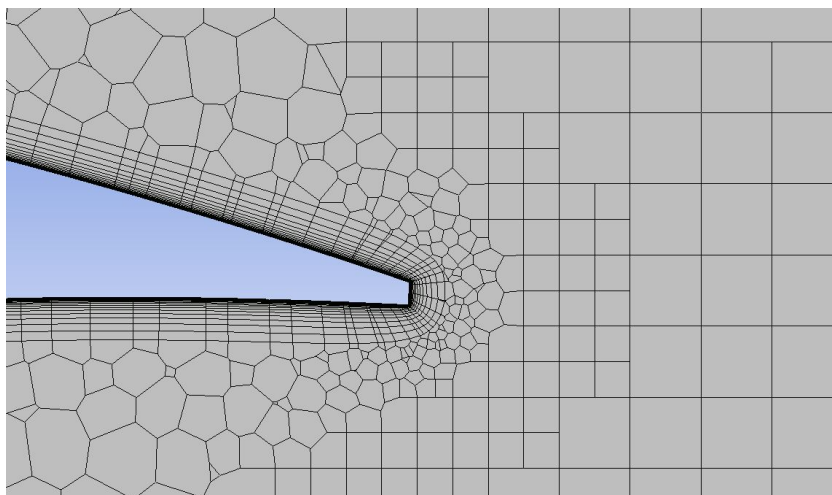


Figure 35: Mesh at trailing edge

5.4. Verification

For the simulation, the created mesh was imported into Ansys Fluent. First, the thing that needed to be done was to validate the simulations. This way done by first performing a mesh convergence study to ensure that the obtained results are not influenced by the mesh. Then multiple turbulence models are compared with data from CIRA to choose which model will be used for all the simulations. Lastly, the pressure coefficient from the simulation will be compared with data obtained from NLR.

5.4.1 Mesh convergence study

Figure 36 shows that with around 17 million elements the lift coefficient starts to converge. A total of 20 million elements are used to ensure accuracy and that the mesh does not influence the results.

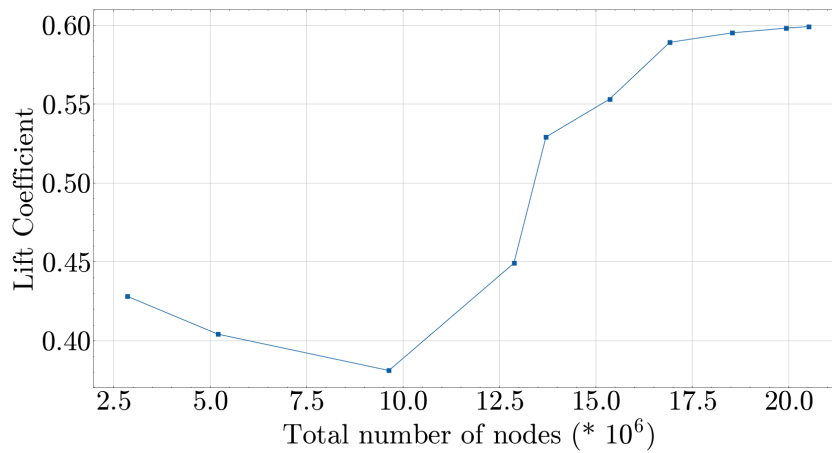


Figure 36: Mesh dependency study for $\alpha = 0.6deg$

5.4.2 Turbulence model

To ensure that the appropriate turbulence model is chosen 3 models are tested namely the Spalart Allmaras, $k - \omega$ standard and the $k - \omega$ SST. These turbulence models are selected because there are numerous studies done on them and proved to be accurate [14] [7]. The $k - \epsilon$ model is not tested since it is known to show poor accuracy for large pressure gradients [6]. The lift and drag calculated from these models were compared to the data that was obtained from CIRA. The following results were obtained:

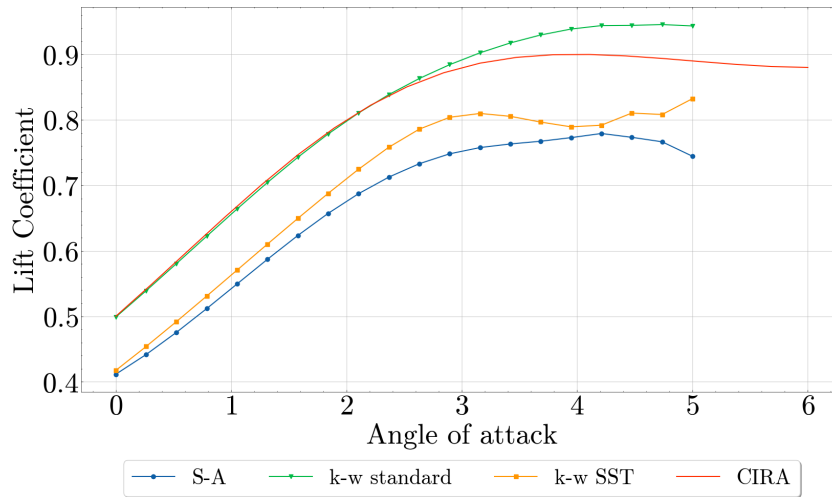


Figure 37: Lift coefficient for various angles of attack and turbulence models are compared to CIRA ³

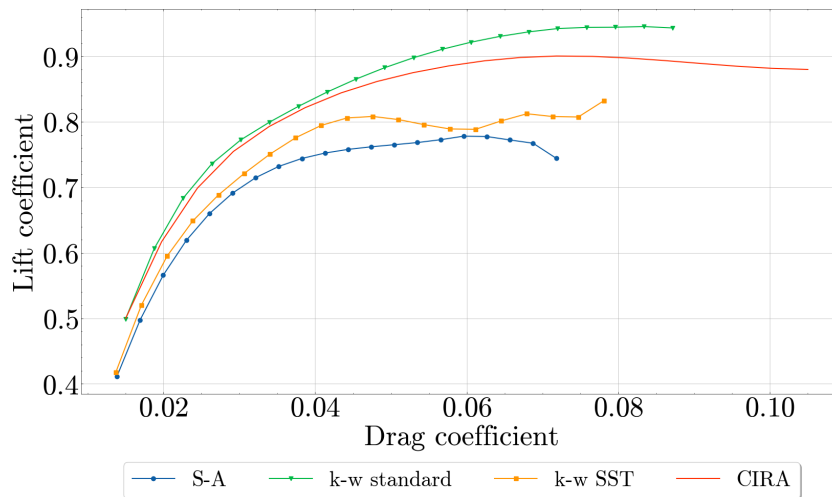


Figure 38: Lift coefficient vs drag coefficient for different turbulence models compared to CIRA

From these results, it became clear that the $k-\omega$ standard model was the most accurate for low angles of attack. The angle of attack in cruise condition is equal to 0.6 degrees. To ensure that this turbulence model produces accurate results the pressure coefficient is also checked in chapter 5.4.3.

³CIRA results are obtained through the CA Upwing project

5.4.3 Validation of pressure coefficient

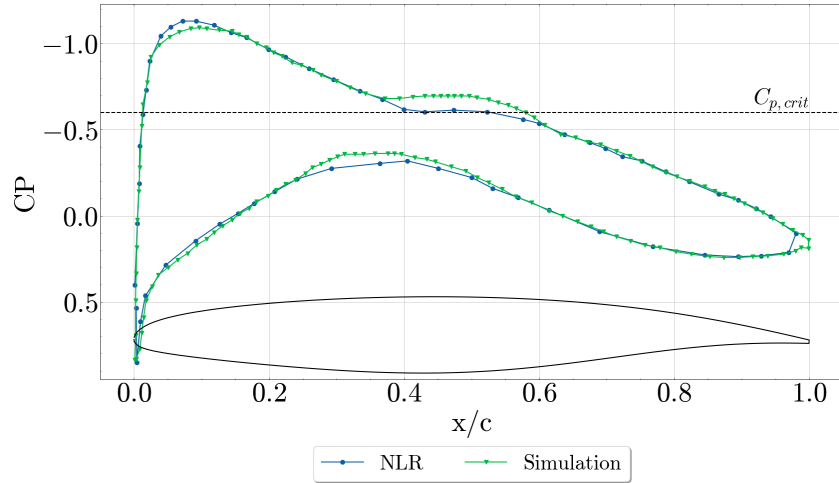


Figure 39: Pressure coefficient comparison between NLR and simulation with turbulence $k-\omega$ standard model with $y/b = 0.62$, for $M_\infty = 0.78$ and $\alpha = 2$ degrees

Figure 39 compares the pressure coefficient of the simulation with the data obtained from NLR. There are some discrepancies between them. Between 40 and 60 percent of the chord length the simulation underpredicts the pressure coefficient. The simulation does however capture the overall trend of the NLR data and in combination with 5.4.2 shows that the $k-\omega$ standard model obtains accurate results and can be used in further simulations. This turbulence model will also be used in the simulations to assess the performance of the mini-tabs.

In the pressure coefficient plot (Fig. 39) the dotted line is equal to the critical pressure coefficient ($C_{p,crit}$) which indicates the beginning or end of a local sonic flow. The following equation [2] is used to calculate the $C_{p,crit}$ which equals to -0.6:

$$C_{p,crit} = \frac{2}{\gamma M_\infty^2} \left(\left(\frac{2}{\gamma+1} \right)^{\frac{\gamma}{\gamma-1}} \left(1 + \frac{\gamma-1}{2} (M_\infty \cos(\Lambda))^2 \right)^{\frac{\gamma}{\gamma-1}} - 1 \right) \quad (32)$$

Given specific parameters including $\gamma = 1.4$, $M_\infty = 0.78$, and $\Lambda = 27.3$, the determination of sonic flow can be recognized by comparing the pressure coefficients with $C_{p,crit}$. This allows for the prediction of local regions with supersonic flow. The dotted line in Fig. 39 which shows the critical pressure coefficient, will also be shown in future pressure coefficient plots, but without the annotation.

5.5. Results

After post-processing in Ansys Polyflow the velocity contour, pressure coefficient and friction coefficient are obtained at cruise conditions. The cruise conditions were set as follows:

Mach number	Angle of attack	Lift coefficient	Flight level
0.78	0.6	0.59	340

Table 4: Cruise conditions for the DLR-F25 wing

To establish a baseline for the mini-tab analysis, the clean wing is analyzed first without any modifications. This initial investigation serves to understand the behavior of the flow around the clean wing.

Figure 40a reveals that the pressure coefficient exceeds the -0.6 critical pressure coefficient indicating a local region of supersonic flow present and that around 60 percent chord-wise position the flow decelerates from supersonic to subsonic speeds. This observation is confirmed by Fig.42 which shows that the velocity exceeds 300 m/s. This velocity is particularly significant as it depicts the speed of sound, or Mach 1. This signifies a local region of supersonic flow. Furthermore, Fig. 41 shows that the flow stays fully attached to the wing since the friction coefficient stays positive along the whole chord.

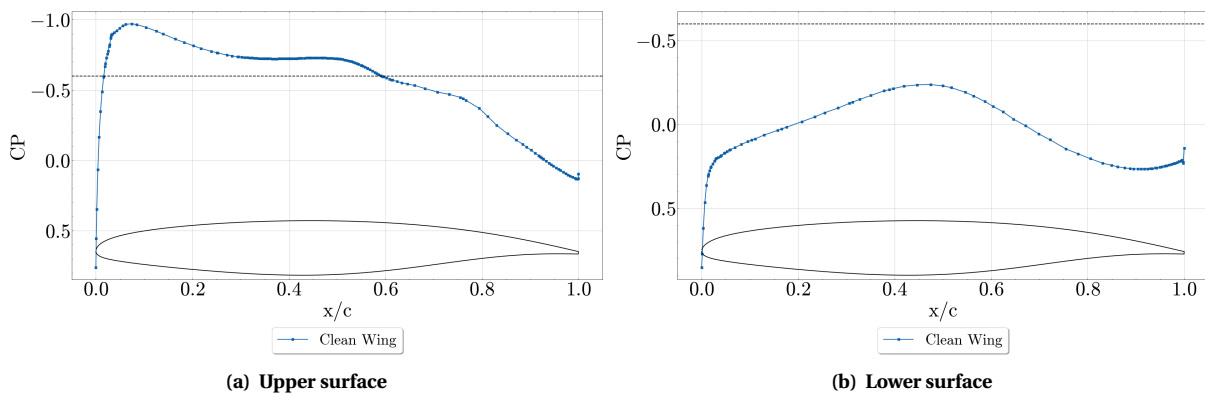


Figure 40: Pressure coefficient along the chord with $y/b = 0.62$, for $M_\infty = 0.78$ and $\alpha = 0.6$ degrees

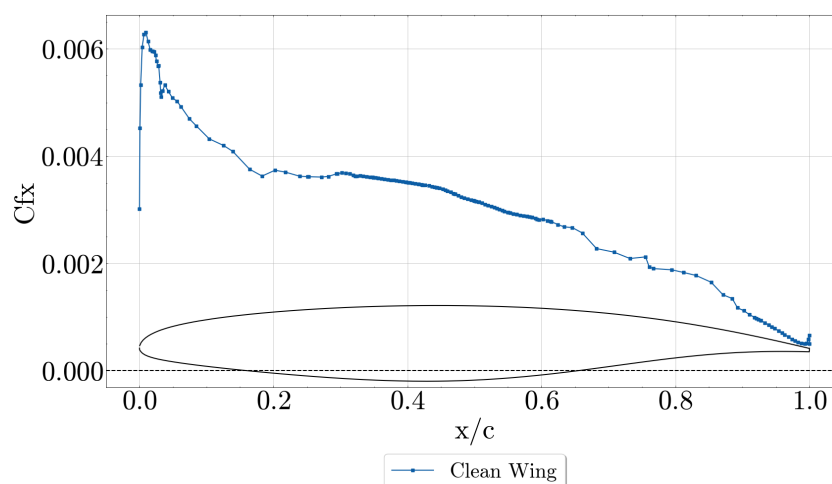


Figure 41: Friction coefficient along the chord of upper surface with $y/b = 0.62$, for $M_\infty = 0.78$ and $\alpha = 0.6$ degrees

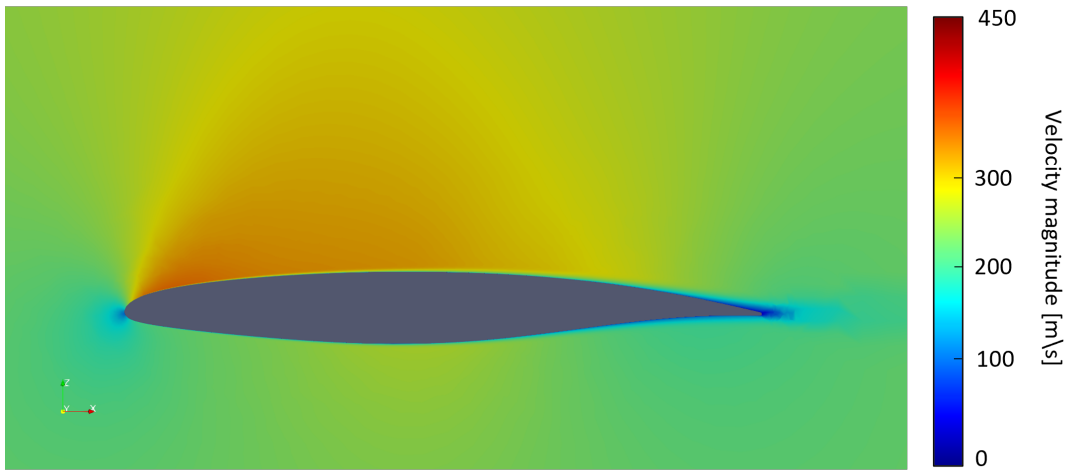


Figure 42: Velocity contour with $y/b = 0.62$, for $M_\infty = 0.78$ and $\alpha = 0.6$ degrees

6

Analysis of the mini-tab effects on lift and drag coefficient

6.1. Introduction

As the analysis transitions from the clean wing to the analysis of mini-tab configurations, the focus shifts to the effects of the mini-tabs on the lift and drag coefficients. The previous chapter studied the fundamental aerodynamic characteristics of the clean wing as a baseline. Now, attention turns to the analysis of mini-tabs and their impact on lift and drag coefficient. By investigating parameters such as height, aspect ratio, span, and chordwise position, the purpose of this chapter is to clarify how the design of mini-tabs affects the performance of the mini-tabs. Table 5 shows the parameters that will be studied and the range of these parameters.

	H/c	AR	x^*/c	y/b
Min	0.015	0.5	0.12	0.62
Max	0.04	24	0.6	0.88

Table 5: The variations in parameters and the respective range

The height parameter is the absolute height of the mini-tab divided by the local chord length. Since the wing is tapered, the local chord length decreases with an increase in the spanwise position. By dividing the height by the local chord length a comparison can be made for different mini-tabs at different spanwise positions while maintaining a constant H/c. The aspect ratio is the length divided by the height of the mini-tab. Int

The geometry and mesh generation of the wing were generated according to the procedure and specifications provided in chapter 5. The $k - \omega$ standard model was chosen for the turbulence modeling since it was proved in chapter 5 to be the most accurate.

The ensure that the flow around the mini-tabs was simulated accurately a Body-of-Influence (BOI) was used. This BOI decreases the element size of the mesh used around the mini-tab. An element size of 2 mm is used to mesh the mini-tabs. The BOI size was set to half the local chord length upstream of the mini-tab and downstream 2 chord lengths. This step was taken to ensure that the wake of the mini-tab is captured accurately.

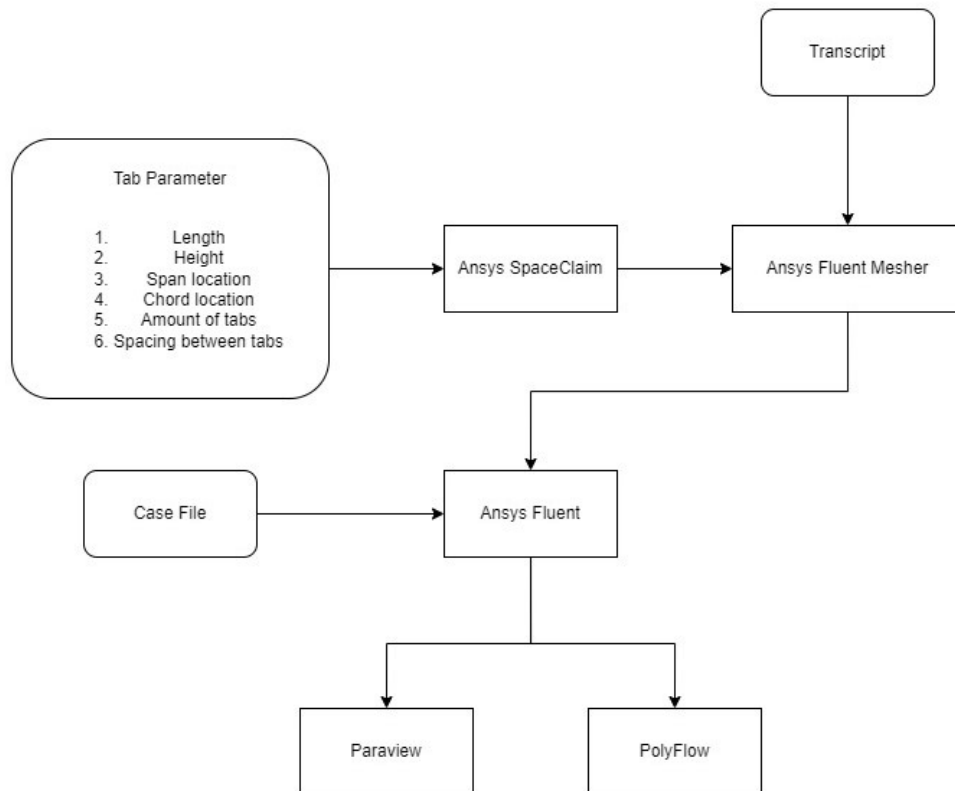


Figure 43: Flowchart for the simulations of the mini-tabs

Figure 43 shows the flowchart of the steps that were taken to simulate the mini-tabs. The case file and transcript were made beforehand to automate the simulations and meshing of the geometries.

In the following chapters, the obtained results will be presented and discussed. Each case will be discussed with the respective velocity contours, pressure coefficients, friction coefficients and streamlines to gain a deeper understanding of the results.

6.2. Comparative analysis of mini-tabs with varied heights and aspect ratios

The initial investigation involved placing the mini-tabs at constant chordwise and span-wise positions, albeit with varying H/c ratios and aspect ratios. Fig.44 shows the sectional lift and drag coefficient for different heights of the mini-tabs and varying aspect ratios. The simulations were performed with an increase of the aspect ratio until the lift section coefficient at the middle of the mini-tabs converged. This was to achieve a 2D-quasi state and reduce the 3D effects.

Figure 44 shows that increasing the aspect ratio of the mini-tabs will let the lift and drag sectional coefficient converge. This convergence is much earlier for larger mini-tabs (eg. $H/c = 0.04$) than smaller mini-tabs (eg. $H/c = 0.015$).

When the mini-tabs with heights $H/c = 0.03$ and 0.04 are compared an interesting thing can be observed. While a bigger aspect ratio is needed for the mini-tab with height $H/c = 0.03$ to reduce the lift generated by the same amount as the mini-tab with height $H/c = 0.04$ (12 for $H/c = 0.03$ and 7 for $H/c = 0.04$, Fig.44), the drag coefficient for the smaller mini-tab is lower. This is also observed when the cases $H/c = 0.025$ and 0.015 are compared with each other. This shows that while a larger mini-tab is more efficient in reducing the lift coefficient, it does however come with a more drag penalty. It might be more beneficial to use a mini-tab with a smaller height to reduce the drag but with an increased aspect ratio to match the lift reduction of the larger mini-tab.

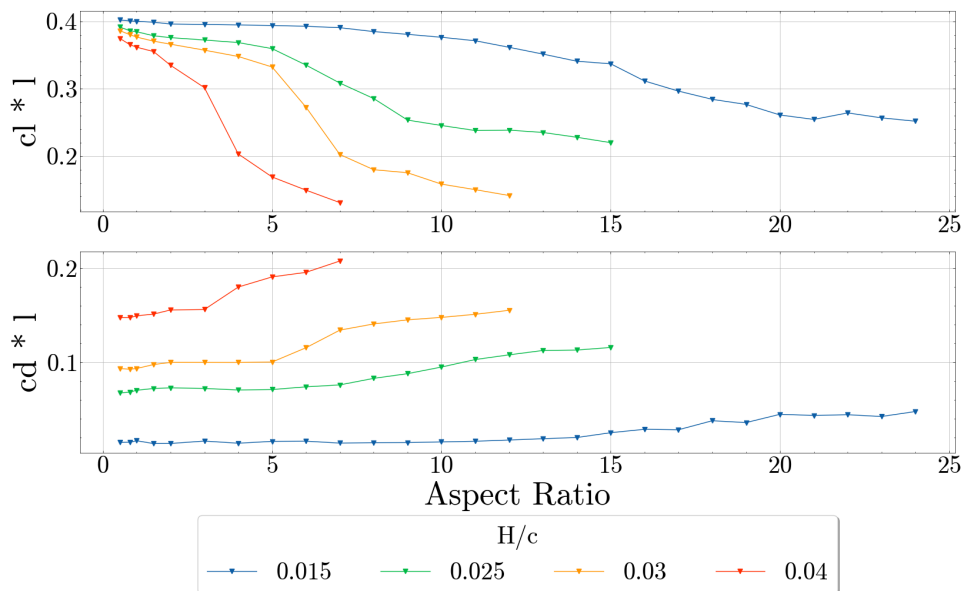


Figure 44: Sectional lift and drag coefficient for different H/c and AR

The following chapters will study the results from Fig.44, focusing specifically on analyzing the impact of changing mini-tab heights while maintaining a constant aspect ratio. This approach allows for a comparative analysis of the mini-tabs, making it easier to have a deeper understanding of their behavior.

I. Analysis of mini-tabs with constant AR of 1

It is observed that the clean wing exhibits a local supersonic region. From the pressure coefficient plot (figure 45a) it can be observed that the introduction of mini-tabs induces shockwave splitting phenomena, causing the original supersonic region of the clean wing to divide into two smaller shockwaves. Examination of the pressure coefficient plot (figure 45a) reveals that at the leading edge, the pressure coefficient is at the beginning similar to the clean wing but a change of the pressure coefficient can eventually be observed. Fig.45a shows that the pressure decreases and crosses

the critical pressure coefficient indicating the onset of a shockwave. After a certain distance, the pressure coefficient increases and crosses the critical pressure coefficient again. This signifies the end of the local supersonic region at the leading edge. This weakening of the shockwave at the leading edge indicates a deceleration of the flow. This will increase the pressure at the upper surface and leads to a reduction of the lift generated and also increases the pressure drag.

Furthermore, an evident correlation appears from Fig.45a, where the increase in pressure at the leading edge correlates with the increase in height of the mini-tab. This increase in the height of the mini-tab will therefore decrease the lift and increase the drag generated. Fig.46 shows this correlation where a smaller shockwave at the leading edge can be observed for an increase in the height of the mini-tab.

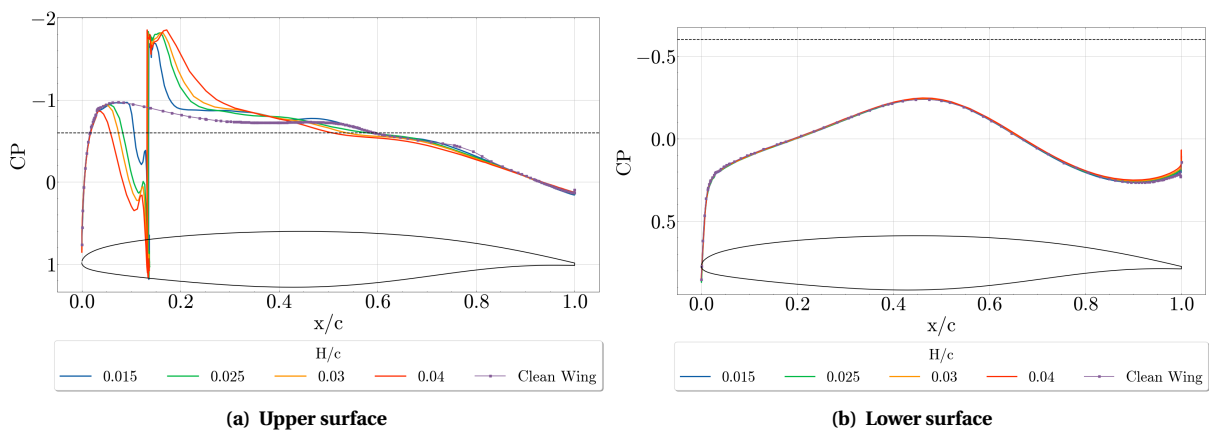


Figure 45: Pressure coefficient along the chord with $y/b = 0.625$, with $AR = 1$, $M_\infty = 0.78$ and $\alpha = 0.6$ degrees with varying H/c

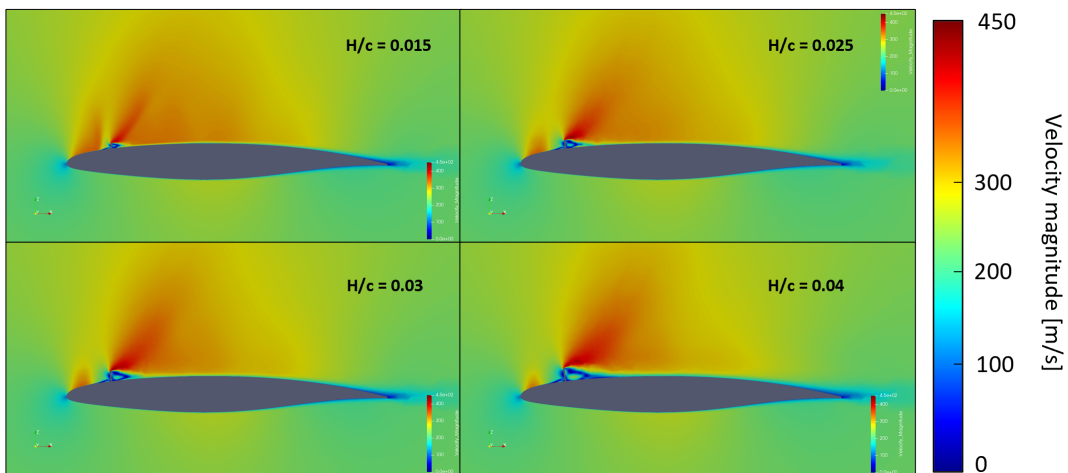


Figure 46: Velocity contour with $y/b = 0.625$, with $AR = 1$, $M_\infty = 0.78$ and $\alpha = 0.6$ degrees with varying H/c

The observed increase in pressure is further highlighted by the vortex region upstream of the mini-tabs, depicted in figures 48 and 47. The vortex region upstream

of the mini-tab gets bigger with an increase in the height of the mini-tab as depicted in Fig.48. In Fig.47 this can be also observed by looking at the value of the friction coefficient. When the value is negative it indicates that the flow is reversed, hence a vortex region. The velocity magnitude depicted in Fig.48 indicates slow-moving air within the vortex region. This slow-moving air corresponds to higher pressure levels, resulting in a decrease in lift generation and increase of the pressure drag.

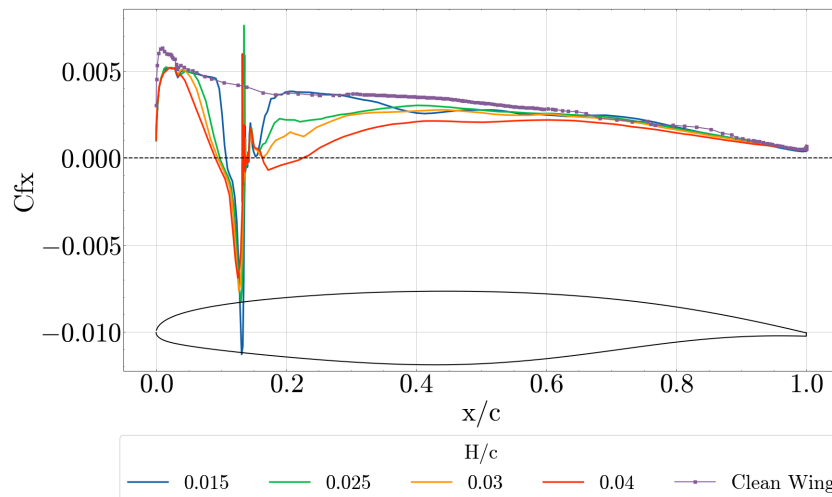


Figure 47: Friction coefficient along the chord of upper surface with $y/b = 0.625$, with $AR = 1$, $M_\infty = 0.78$ and $\alpha = 0.6$ degrees with varying H/c

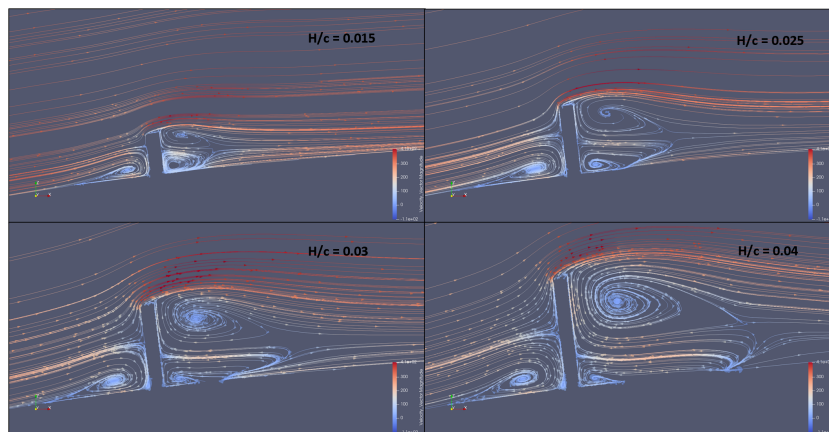


Figure 48: Streamlines with $y/b = 0.625$, with $AR = 1$, $M_\infty = 0.78$ and $\alpha = 0.6$ degrees with varying H/c

The relationship between mini-tab height and flow reattachment is analyzed, explaining changes in pressure distribution and their implications for lift and drag characteristics. The mini-tabs create a circulation zone downstream that gets larger with an increase in height which can be seen from figures 48 and 47. An intrinsic flow can be observed where not one but 2 vortices are being created. One at the upper side of the mini-tab and another one at the lower side. The flow does eventually reattach itself to the wing in all cases, this reattachment is delayed with increasing mini-tab

height, as observed by the larger negative region of the friction coefficient observed in Fig.47. The separated flow introduces more turbulent and low-energy air behind the mini-tab, which adversely affects the lift generated by the wing and increases the drag.

Another consequence of the higher pressure at the leading edge is that the apparent angle of attack changes. Because of this higher pressure, more flow is redirected towards the lower side of the wing. This accelerates the flow and can be seen from Fig.45b where a decrease of the pressure coefficient can be observed for an increase of the height of the mini-tabs. The reduction of pressure at the lower side of the wing decreases the lift generated by the wing.

II. Analysis of mini-tabs with constant AR of 5

Figure 49a shows that in comparison with Fig.45a, the mini-tabs with an height $H/c \geq 0.03$ show no shockwave at the leading edge anymore. This is depicted by Fig.49a which shows that the mini-tabs with $H/c \geq 0.03$ do not cross the critical pressure coefficient at the leading edge. This is also confirmed by Fig.50 where the velocity at the leading edge for the mini-tabs of $H/c = 0.03$ and 0.04 does not exceed 300 m/s which is the equivalent of Mach 1. These findings show that increasing the aspect ratio has the same effect as increasing the height of the mini-tabs in that, it increases the pressure at the leading edge which decreases the lift and increases the pressure drag. This is confirmed by Fig.44 which shows that an increase in the aspect ratio decreases the lift and increases the drag generated.

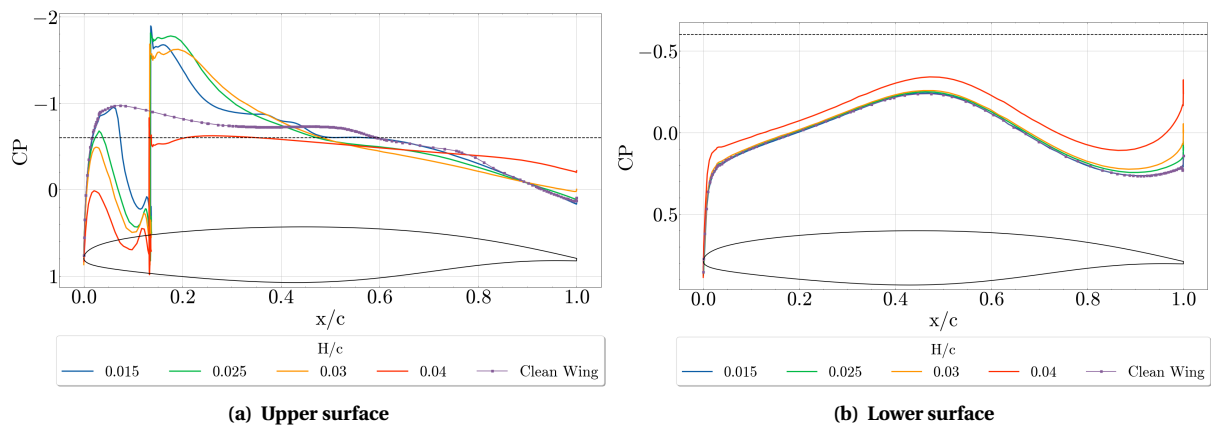


Figure 49: Pressure coefficient along the chord with $y/b = 0.625$, with $AR = 5$, $M_\infty = 0.78$ and $\alpha = 0.6$ degrees with varying H/c

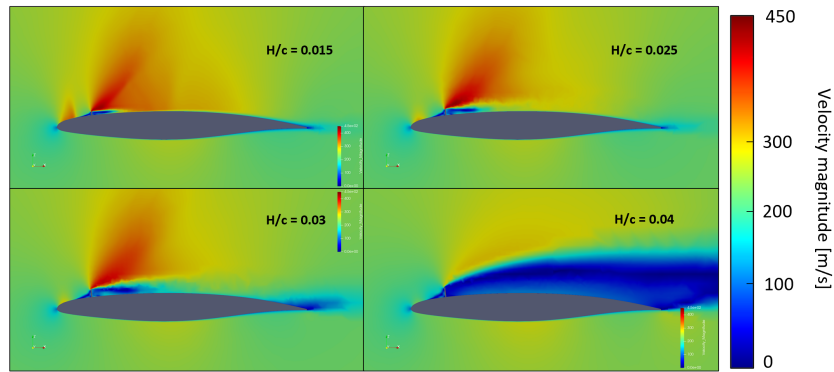


Figure 50: Velocity contour with $y/b = 0.625$, with $AR = 5$, $M_\infty = 0.78$ and $\alpha = 0.6$ degrees with varying H/c

In addition to the higher pressure at the leading edge, the flow behind the mini-tabs exhibits significant variations. Fig.49a shows that the pressure drop for the mini-tab with a $H/c = 0.04$ is reduced across the mini-tab accompanied by a higher pressure coefficient after the mini-tab when compared to the other cases. It becomes more apparent what happens when examining figures 50 and 51.

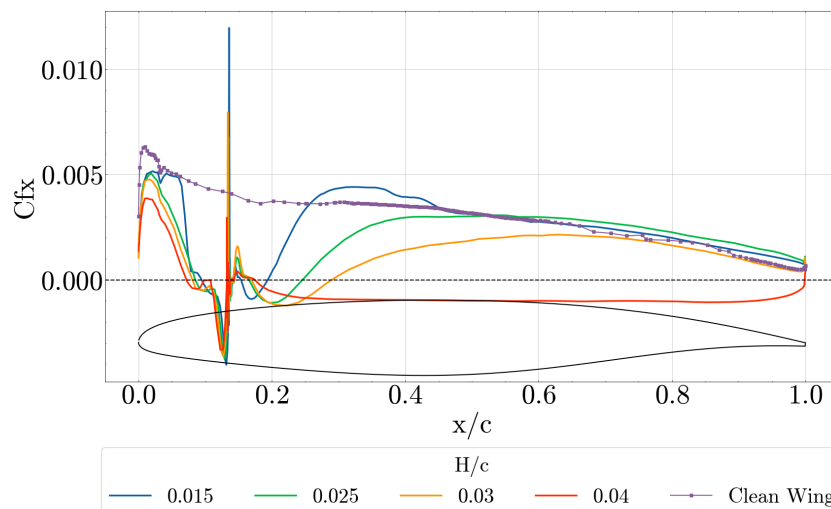


Figure 51: Friction coefficient along the chord of upper surface with $y/b = 0.625$, with $AR = 5$, $M_\infty = 0.78$ and $\alpha = 0.6$ degrees with varying H/c

From Fig.51 it can be observed that the friction coefficient after the mini-tab with $H/c = 0.04$ is negative which indicates a reversed vortex flow. This would explain the higher pressure coefficient that was observed in Fig.49a since a reversed flow is often characterized by low-energy and low-velocity flows. Figures 50 and 52 provide further insights, which show a wake that is completely detached from the wing after the mini-tab. This low-energy and turbulent flow decreases the lift generated by the wing.

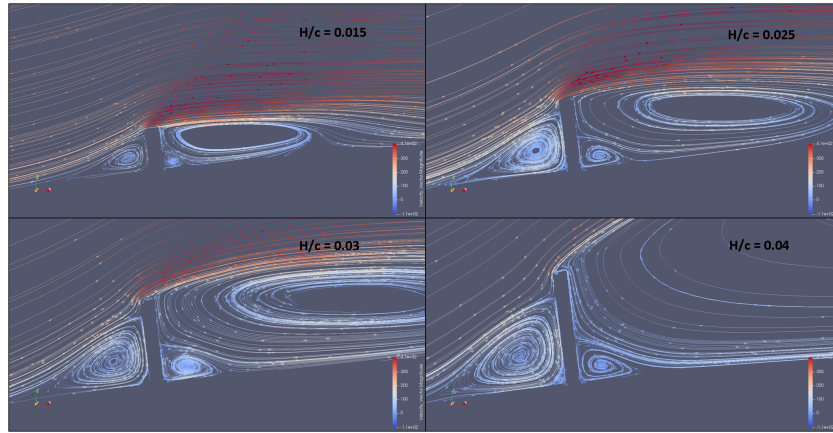


Figure 52: Streamlines with $y/b = 0.625$, with $AR = 5$, $M_\infty = 0.78$ and $\alpha = 0.6$ degrees with varying H/c

For the case of $H/c = 0.03$ the flow after the mini-tab reattaches itself but a wake is still created at the trailing edge. This might indicate that the flow is beginning to detach itself from the wing completely as in the case of $H/c = 0.04$. Moreover, if the pressure drop across the mini-tab with a height of $H/c = 0.04$ is compared with figures 45a and 49a something can be observed. For the mini-tab of $AR = 1$ and $H/c = 0.04$, the pressure drop is decreased compared to the mini-tabs with the same AR . At $AR = 5$, this mini-tab shows a complete detachment of the flow after the mini-tab. This might indicate that from the pressure coefficient plots alone a prediction can be maybe made when the mini-tab is on the verge of complete detachment. The same can be seen in Fig.49a for the case of $H/c = 0.03$ where the pressure drop is also decreased. This claim is supported by 50 where a larger wake is observed when compared to the smaller mini-tabs.

Figure 49b shows that the pressure coefficient at the lower side of the wing decreases with an increase in the height of the mini-tab. This was observed also for the case with $AR = 1$ (figure 45b). For the case of $AR = 5$ the differences between the pressure coefficients of the varying heights are more pronounced when compared to the $AR = 1$ case. This shows that increasing the aspect ratio decreases the pressure at the lower side of the wing which in extent reduces the lift induced by the wing.

III. Analysis of mini-tabs with constant AR of 7

Figure 53a illustrates that the area of local supersonic flow vanished for $H/c \geq 0.025$ at the leading edge. This trend mirrors observations from previous cases ($AR = 1$ and $AR = 5$), where increasing the aspect ratio results in a smaller and weaker shockwave at the leading edge. Consequently, the lift produced at the leading edge decreases with an increase in AR and height. Even for small heights such as $H/c = 0.025$, lift reduction can be attained by an increased aspect ratio.

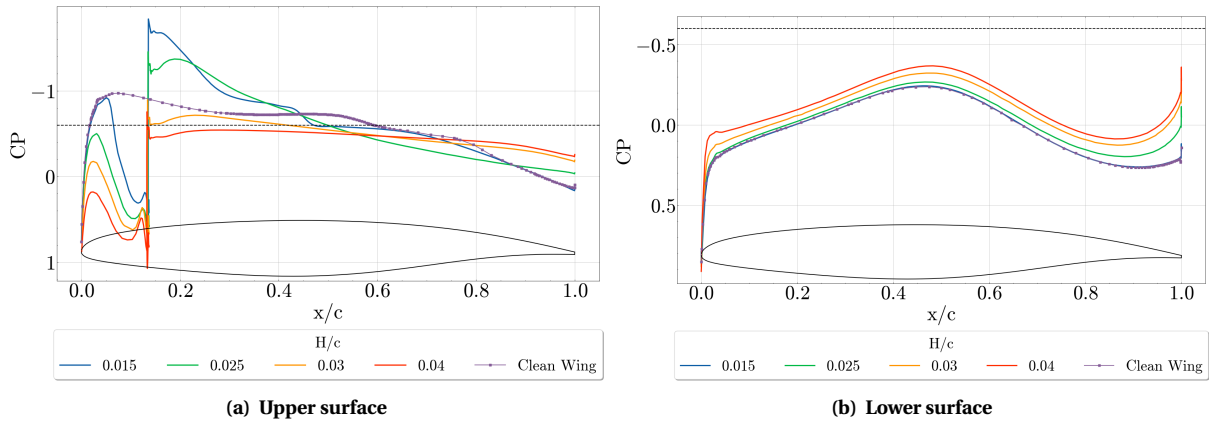


Figure 53: Pressure coefficient along the chord with $y/b = 0.625$, with $AR = 7$, $M_\infty = 0.78$ and $\alpha = 0.6$ degrees with varying H/c

It was mentioned in chapter II. that the flow behind the mini-tab for the height $H/c = 0.04$ was detached and that the same was happening for the mini-tab $H/c = 0.03$. When looking at figures 55 and 54 it can be observed that the flow after the mini-tab is completely separated. Fig.55 indicates this through the friction coefficient behind the mini-tab, indicating a negative value extending from the mini-tab location to the trailing edge. This indicates a completely detached and reversed flow behind the mini-tab. Figures 54 and 56 also support this observation where a detached wake can be seen for the mini-tabs with heights $H/c = 0.03$ and 0.04 . This detached wake will reduce the lift generated by the wing.

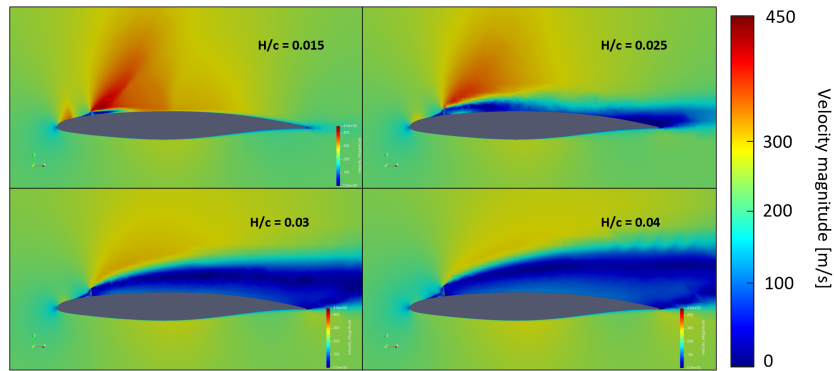


Figure 54: Velocity contour with $y/b = 0.625$, with $AR = 7$, $M_\infty = 0.78$ and $\alpha = 0.6$ degrees with varying H/c

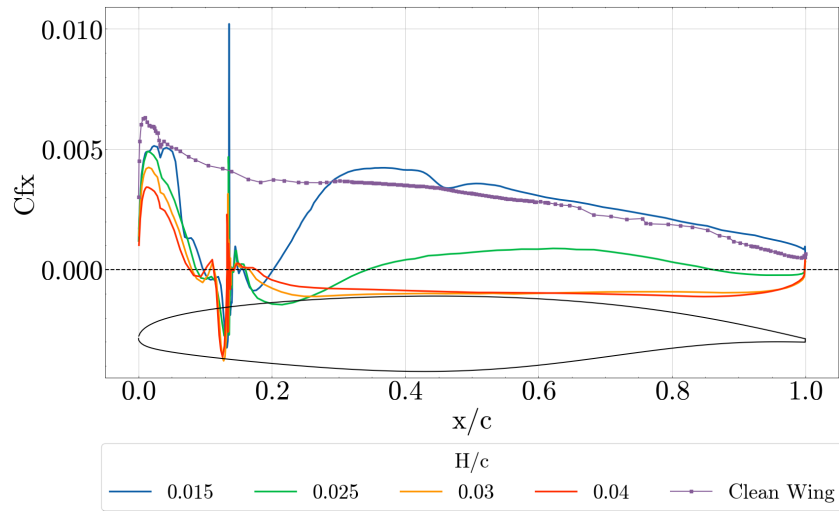


Figure 55: Friction coefficient along the chord of upper surface with $y/b = 0.625$, with $AR = 7$, $M_\infty = 0.78$ and $\alpha = 0.6$ degrees with varying H/c

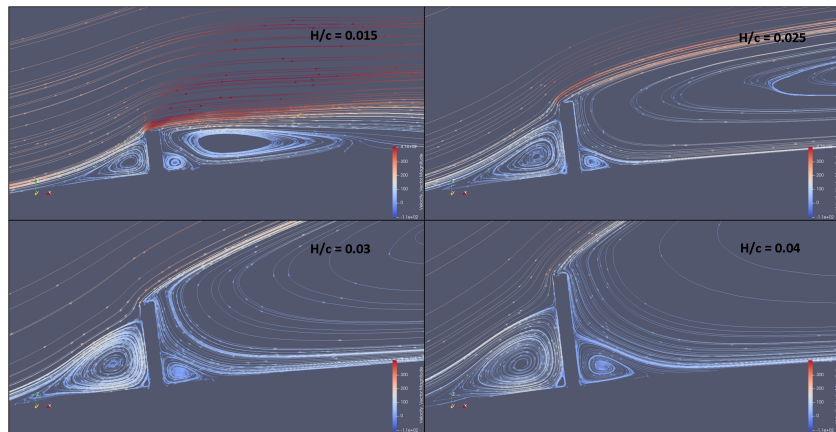


Figure 56: Streamlines with $y/b = 0.625$, with $AR = 7$, $M_\infty = 0.78$ and $\alpha = 0.6$ degrees with varying H/c

As was the case in chapter II, where it was theorized from the velocity contour (figure 50) and pressure coefficient plot (figure 49a) that the flow behind the mini-tab with a height $H/c = 0.03$ was on the verge of separating, the same can be said for the case of the mini-tab $H/c = 0.025$. Fig.54 shows that for this mini-tab the wake is close to separating entirely. Fig.55 also shows that the flow is first reversed behind the mini-tab, reattaches to the wing and then detaches again. As was mentioned earlier the separated, low-energy and turbulent flow reduces the lift generated.

Figure 53b indicates that the velocity at the lower side of the wing is accelerated. When compared to Fig.49b it becomes clear that an increase in the aspect ratio increases the acceleration at the lower side of the wing and in extent reduces the pressure at the lower side of the wing and in extent the lift. This acceleration of the flow at the lower surface was also observed in previous cases. This acceleration of the flow will also increase the friction drag.

6.3. Chordwise position of the mini-tab

Placing the mini-tab closer to the trailing edge decreases the pressure drop which is observed in Fig.57a. Fig.58 illustrates this by depicting the reduction in the size of the shockwave at the mini-tab. This will reduce the re-energizing effect that the local supersonic region has on the wake behind the mini-tab. This will make the wake more prone to detach from the wing and disrupt the airflow behind the mini-tab, hence decreasing the lift generated.

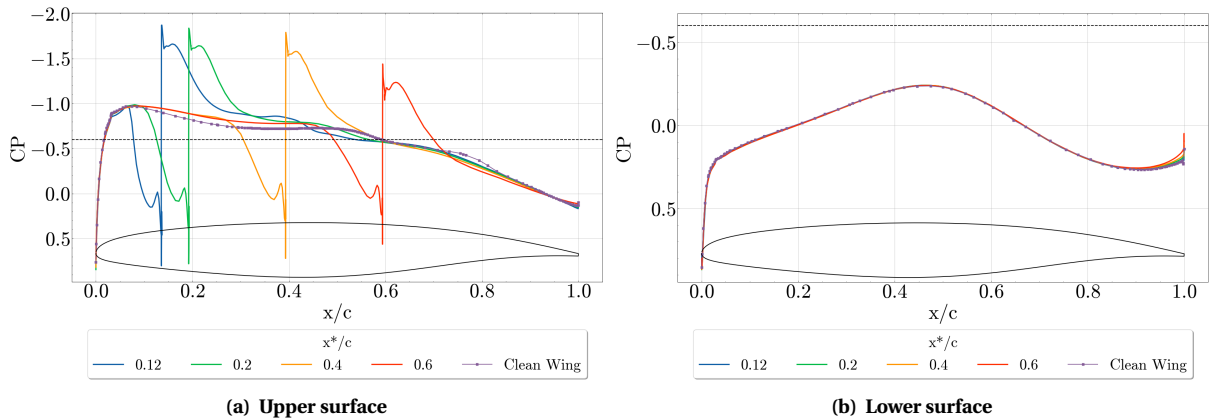


Figure 57: Pressure coefficient along the chord with $y/b = 0.62$, with $AR = 4$, $H/c = 0.015$, for $M_\infty = 0.78$ and $\alpha = 0.6$ degrees

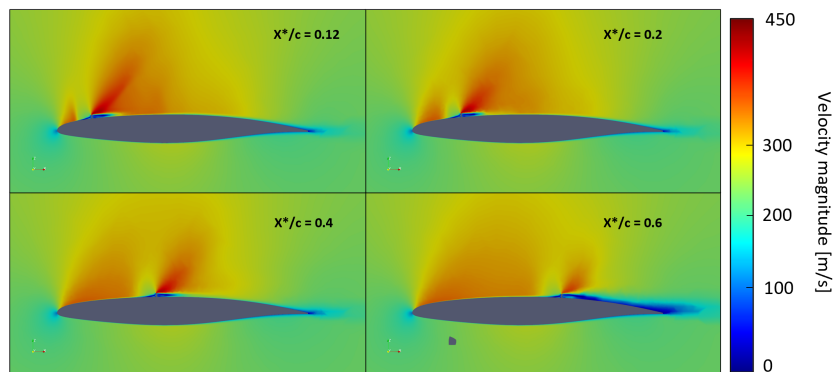


Figure 58: Velocity contour with $y/b = 0.625$, with $AR = 4$, $H/c = 0.015$, for $M_\infty = 0.78$ and $\alpha = 0.6$ degrees

When comparing the pressure coefficients (as shown in Fig.57) along the surfaces for x/c values of 0.12 and 0.6, several differences emerge. For the case $x^*/c = 0.12$ the pressure coefficient initially matches the clean wing at the leading. As the mini-tab is approached, the pressure coefficient rises, indicating an increase in pressure upstream of the leading edge. After the mini-tab, the pressure coefficient drops where Fig.59 shows that there is a region of reversed flow downstream of the mini-tab. This drop in pressure coefficient also indicates the formation of a new shockwave downstream of the mini-tab, which is evident from Fig.58.

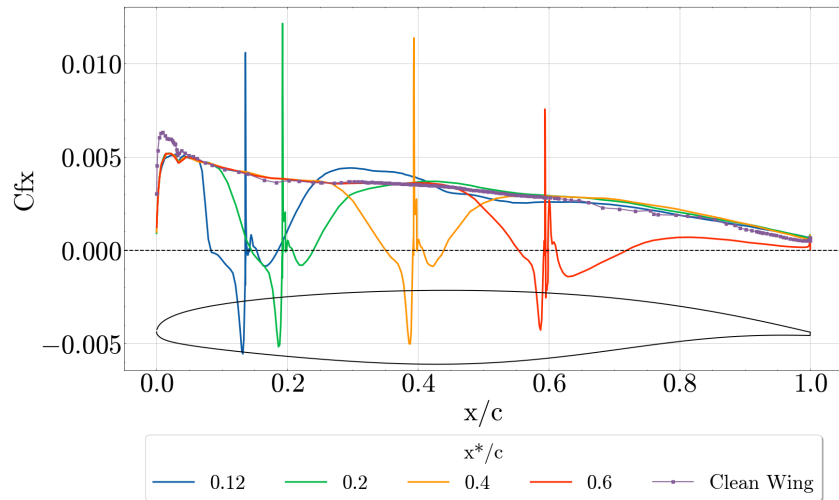


Figure 59: Friction coefficient along the chord of upper surface with $y/b = 0.62$, with $AR = 4$, $H/c = 0.015$, for $M_\infty = 0.78$ and $\alpha = 0.6$ degrees

For the case of $x^*/c = 0.6$ the increase of the pressure coefficient upstream of the mini-tab happens earlier when compared to the mini-tab placed at $x^*/c = 0.12$. This larger region of pressure at the leading edge explains why the lift reduction is more pronounced for the mini-tab placed at $x^*/c = 0.6$.

6.4. Spanwise position of the mini-tab

The mini-tabs position was varied along the span of the wing, maintaining a consistent absolute height for each case. However, due to the tapering chord length of the wing towards its tip, the ratio of the mini-tab height to the local chord length (H/c) increases as the mini-tab is positioned closer to the wing's tip. Fig.60 illustrates the results obtained from this variation. It shows that placing the mini-tab closer to the tip (increase of y/b) reduces the lift coefficient and increases the drag generated.

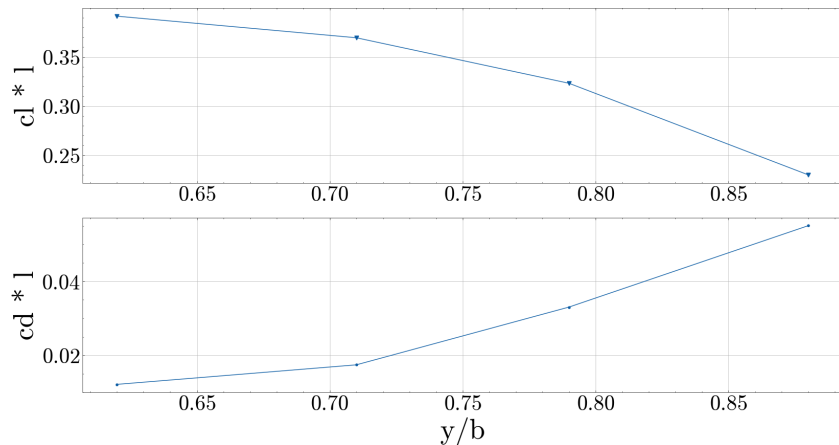


Figure 60: Lift and drag section coefficients results for different spanwise positions

While the absolute height is the same for all cases, the effective height, defined as H/c , increases when the mini-tabs are placed closer to the tip. This increase in relative height is

attributed to the tapering chord length of the wing towards its tip, causing the mini-tab to appear relatively taller as it approaches the tip.

As the mini-tab gets relatively higher, the shockwave at the leading edge becomes smaller and weaker as observed in Fig.61a where the region of the pressure coefficient that surpasses the critical pressure coefficient gets smaller. For the case of when the mini-tab is placed at $y/b = 0.88$, the shockwave is absent. This absence is also shown in Fig.62 where no shockwave can be observed at the leading edge for the mini-tab placed at 88% of the span of the wing. Moreover, Fig.61a confirms this observation by showing a pressure coefficient at the leading edge that does not cross the critical pressure coefficient of -0.6, indicating a local subsonic flow. This deceleration of the flow at the leading edge, resulting from the weakening of the shockwave, leads to a reduction of the lift and increases the drag generated. These findings of the diminishing of the shockwave at the leading edge align with the trends observed in previous simulations, such as those described in section 6.2. However, This is not surprising since the H/c increases when the mini-tab is positioned closer to the wingtip so it should have the same effect as increasing the absolute height of the mini-tab at a fixed wingspan.

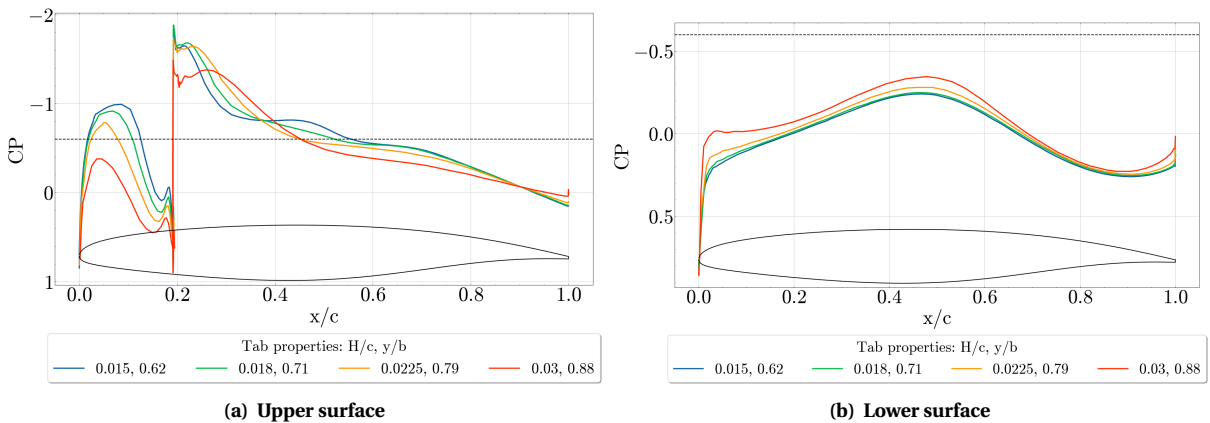


Figure 61: Pressure coefficient along the chord at different spanwise distance for $M_\infty = 0.78$ and $\alpha = 0.6$ degrees

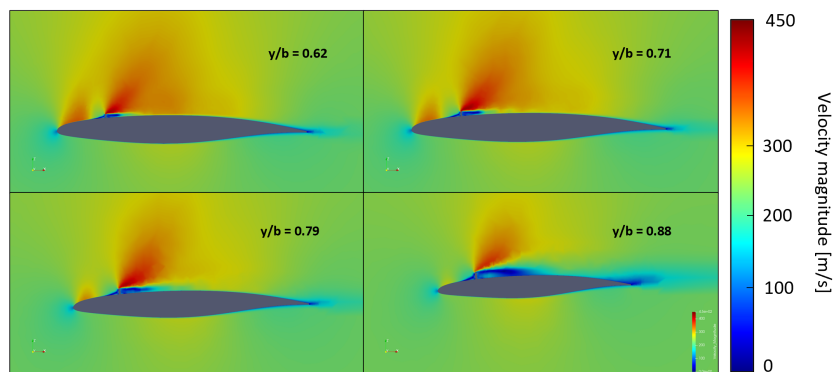


Figure 62: Velocity contour at different spanwise distance for $M_\infty = 0.78$ and $\alpha = 0.6$ degrees

When analyzing Fig.61a, it is observed that for the mini-tab placed at $y/b = 0.88$, the

pressure drop is reduced across the mini-tab when compared to the other cases. This was encountered numerous times when looking at section 6.2 where a significant decrease in pressure drop indicates that the flow behind the mini-tab is on the verge of separating from the wing. Section 6.2 delved into the effects of varying the height of the mini-tab at fixed spanwise positions. According to the current analysis, a decrease in pressure drop across the mini-tab aligns with the hints of potential flow separation discussed in section 6.2. The observation of the wake enlargement again mirrors the trends observed in previous simulations, such as those described in section 6.2.

By understanding the effects of this reduced pressure drop, we can speculate that the airflow behind the mini-tab may be approaching a critical condition where it detaches from the wing surface. This separation disrupts the smooth flow pattern, leading to turbulence and vortices that can increase drag and reduce lift. Moreover, an enlarged region of reversed flow downstream of the mini-tab, as shown in Fig.63 for the case of $y/b = 0.88$, reinforces this observation of flow separation.

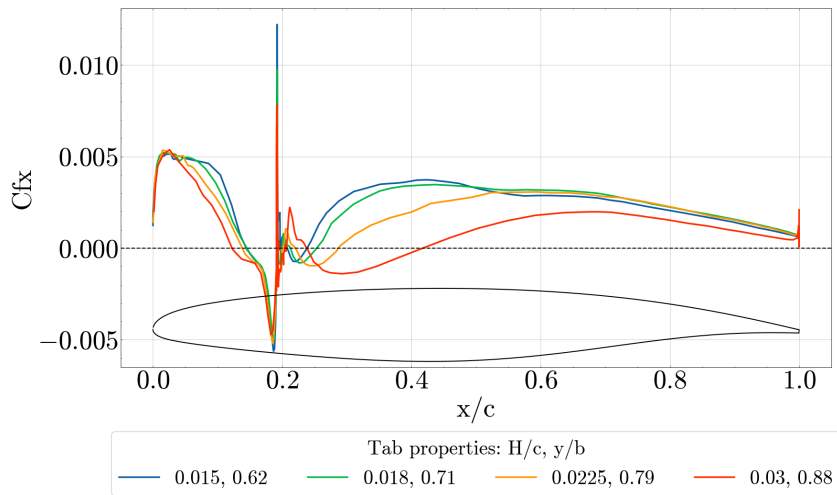


Figure 63: Friction coefficient along the chord of upper surface at different spanwise distance for $M_\infty = 0.78$ and $\alpha = 0.6$ degrees

These findings of the diminishing of the shockwave at the leading edge and wake enlargement align with the trends observed in previous simulations, such as those described in section 6.2, where variations in mini-tab height were explored at fixed spanwise positions. This is not surprising however since as mentioned before the H/c increases when the mini-tab is positioned closer to the wingtip.

6.5. Comparative analysis of mini-tabs at different spanwise locations with constant H/c

Building upon the previous investigation into the effects of mini-tabs at varying spanwise positions, this chapter delves deeper into the impact of their placement along the wing. The analysis now compares two mini-tabs positioned at different locations but with identical H/c , unlike the previous analysis where the spanwise positioning varied but with also different H/c .

In this chapter two mini-tabs are compared with a constant $H/c = 0.03$, $AR = 4$ and $x^*/c = 0.15$. The only difference is the spanwise location in which they are placed. One is placed at 62 % and the other one at 88 %. By maintaining uniform geometric parameters and only varying the spanwise location, this investigation aims to determine any differences in performance attributed to their placement along the span.

Figure 64 shows that despite the same geometrical properties there is quite a difference between the mini-tabs. The first noticeable thing is the pressure drop along the mini-tab. The mini-tab positioned closer to the wingtip experiences a decrease in pressure drop compared to the mini-tab placed at $y/b = 0.62$. Furthermore, as depicted in Fig.65, this mini-tab experiences a larger region of separated flow when compared to the mini-tab placed at $y/b = 0.62$. This larger region of separated flow experienced by the mini-tab placed at 88% indicates a more pronounced reduction in lift compared to the other mini-tab.

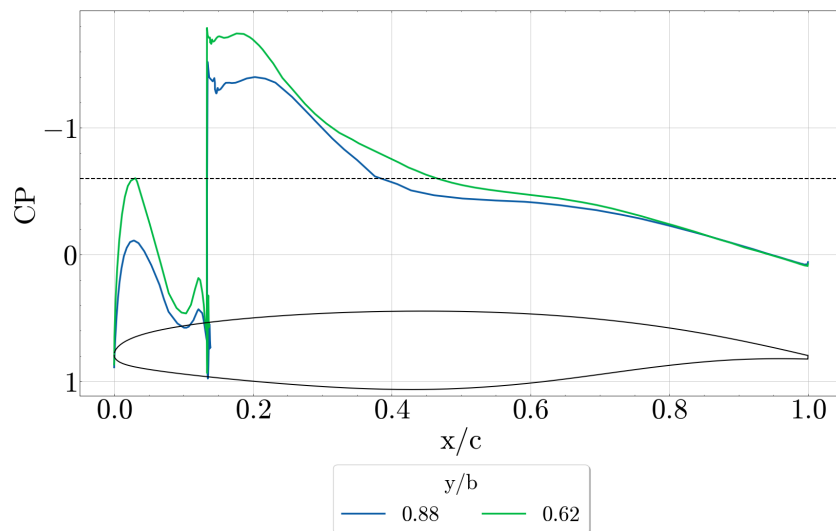


Figure 64: Pressure coefficient along the chord of upper surface at different spanwise positions and $H/c = 0.03$, $AR = 4$ and $x^*/c = 0.15$

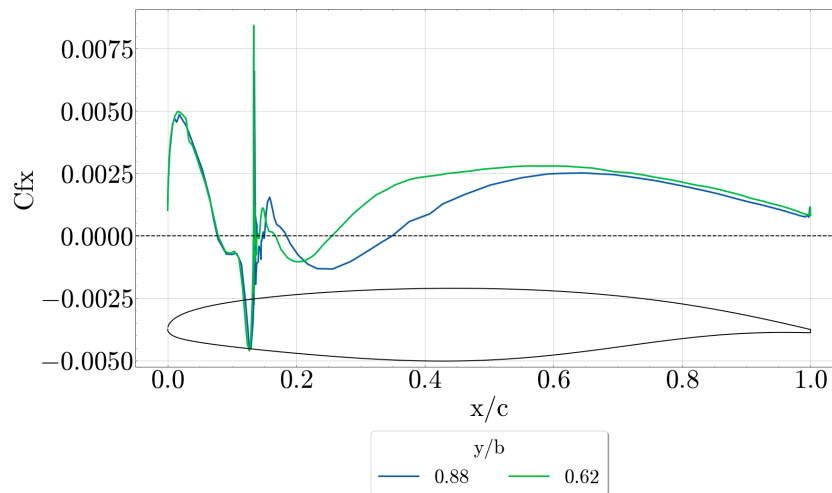


Figure 65: Friction coefficient along the chord of upper surface at different spanwise positions and $H/c = 0.03$, $AR = 4$ and $x^*/c = 0.15$

The comparative analysis further highlights the differences in pressure coefficients at the leading edge between the two cases. The comparison between the two cases shows that the mini-tab positioned closer to the wingtip experiences a higher pressure coefficient at the leading edge compared to the one at 62% spanwise position. This elevated pressure coefficient signifies a more significant deceleration and higher-pressure region, resulting in a more pronounced reduction in the lift generated by the wing.

This discrepancy between the 2 mini-tabs is caused by the two different wing shapes at the different spanwise locations. The wing shape is not constant over the whole spanwise direction. The closer it gets to the tip the lower the local AOA. This is often done to reduce the lift generated by the wing and in extent reduce the bending moment. The same is happening for this wing. While the geometrical properties of the mini-tabs are the same, the wing shape is not. This does impact the results, unfortunately. This can also be seen in Fig.64 where a higher pressure is found at the leading edge for the mini-tab closer to the tip. As stated the angle of attack angle is lower for this location and this should in extent reduce the acceleration and increase the pressure at the upper surface of the wing which is observed.

6.6. Analysis of multi-tab configuration performance

In this study, an investigation was carried out to examine the interaction of multiple mini-tabs when placed on a wing. To ensure a proper comparison, an absolute height of 0.03 meters and a chordwise position of $x^*/c = 0.2$ was set constant for all mini-tabs. However, the spanwise locations and aspect ratios of the mini-tabs were varied for every simulation. Specifically, they were positioned between $0.62 \leq y/b \leq 0.88$ of the wingspan.

To ensure a fair comparison between mini-tab configurations with different aspect ratios, a new non-dimensional parameter called the wall ratio was introduced. This metric quantifies the proportion of the wing's span covered by the mini-tabs relative to the span distance between $0.62 \leq y/b \leq 0.88$. For example, when 2 different configurations of AR

= 2.5 and 10 are compared, achieving the same wall ratio means that the configuration of $AR = 2.5$, would require 4 times more mini-tabs compared to the other case to cover the same wingspan. Making the wall ratio a constant between the different configurations and in extent of the area that the mini-tabs cover, allows for a meaningful comparison.

The simulations were categorized into two groups based on the orientation of the mini-tabs (figure 66a). In one set of simulations, the mini-tabs were oriented orthogonal to the incoming airflow (figure 66b), while in the other set, they were aligned along the 20 percent chordwise line (figure 66c). This approach allowed us to investigate how different orientations may influence the aerodynamic behavior of the mini-tabs and their interaction with the wing.

Three different aspect ratios of 2.5, 5 and 10 were simulated with varying wall ratios and different mini-tab orientations. In the initial simulations, the mini-tabs were placed perpendicular to the free-stream wind ($\theta = 0^\circ$), as illustrated by Fig.66b. Fig.67 displays the results of these simulations for varying wall ratios. Additionally, the dotted line in Fig.67 ($CL \approx 0.5$) represents a simulation that was performed with a continuous mini-tab that spans the entire length of the domain between $0.62 \leq y/b \leq 0.88$. The single-tab simulation was performed to function as a baseline for comparison with the multi-tab configurations. Given that this continuous mini-tab covers the entire spanwise range of $0.62 \leq y/b \leq 0.88$, its resulting lift coefficient is expected to be the lowest. By comparing this result with the other simulations for different wall ratios it would be a good measure of how efficient the multi-tab configuration is.

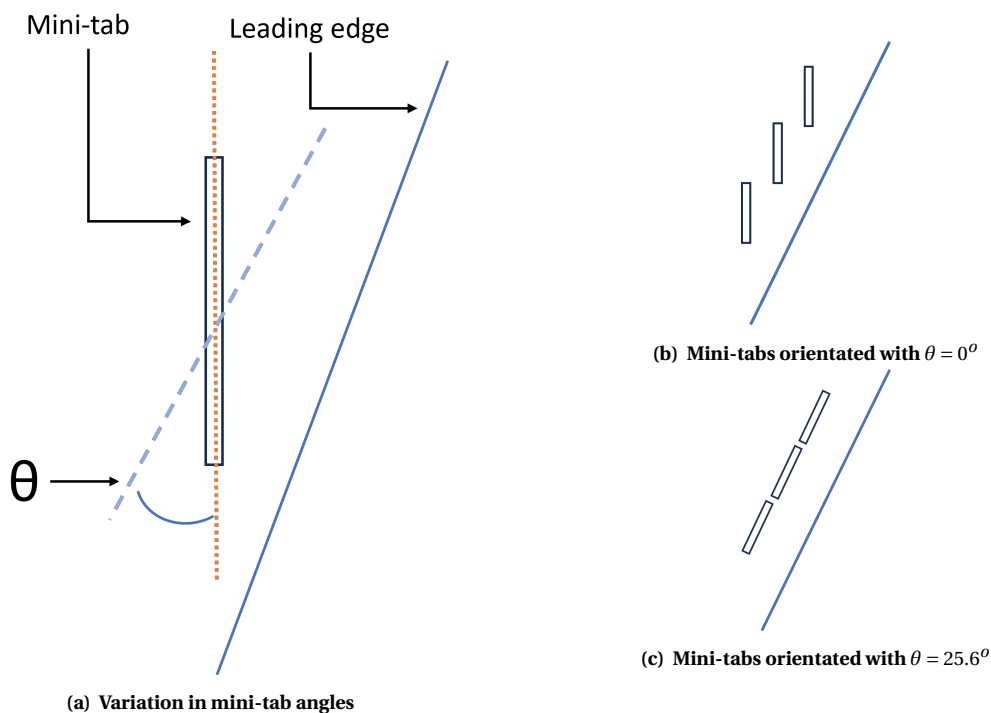


Figure 66: Definition of different orientations of the mini-tab

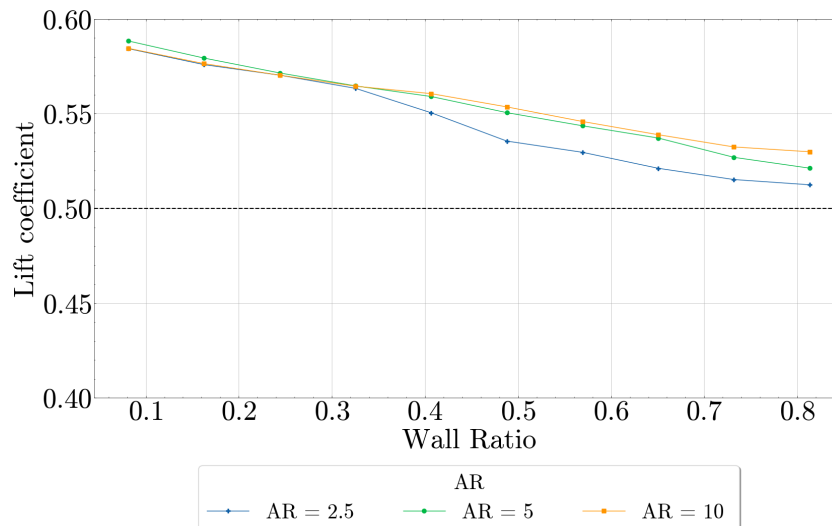


Figure 67: Lift coefficient for different Wall ratio's and AR with $\theta = 0^\circ$

In Fig.67, the lift coefficients from the simulations with varying wall ratios are presented. As depicted in Fig.67, the lift coefficient decreases as the wall ratio increases for all aspect ratios, aligning with expectations. With more mini-tabs placed on the wing, the more influence the mini-tabs will have on the performance of the wing. It can be seen that for low wall ratios, the differences between the mini-tab configurations with different aspect ratios are negligible. At around a wall ratio of 0.3, a difference is observed where the lift coefficient of the configuration of AR = 2.5 drops faster than the other cases.

The explanation lies in the orientation of the mini-tabs. Placing the mini-tabs in such a way will create gaps between the mini-tabs in the chord-wise direction. Figures 66b and 68 show how the mini-tabs are placed for $\theta = 0^\circ$. Since the wing is swept and the chord-wise position of the mini-tabs is constant at $x^*/c = 0.2$ there is a gap between them as mentioned. These gaps allow airflow, leading to wake energization. As mentioned in earlier chapters, a correlation has been shown between the separated flow behind the mini-tab and the reduction in lift. As the area of separated flow increases, the flow becomes more turbulent and loses energy, leading to a decrease in lift. Because of the wake energization this separated region gets smaller and the reduction of lift will be less pronounced. This does decrease the performance of the mini-tabs.

This effect becomes more pronounced at higher wall ratios as can be seen from Fig.67. It shows that the differences between the configurations with varying AR increase with the increase of the wall ratio. The reason for this observation is that for mini-tabs with a low aspect ratio like AR = 2.5, the amount of mini-tabs needed is four times more when compared to the mini-tabs with AR = 10 for a constant wall ratio. This will reduce the gaps between the mini-tabs and will also reduce the lift generated by the wing.

Another observation from Fig.67 is that the lift coefficient of all three cases seems to converge for high wall ratios above the simulation for the continuous tab that achieved a

lift coefficient of around 0.5. This suggests a reduction in performance across the multi-tab configurations. This would support the idea that the gaps between the mini-tabs reduce the performance and that orientating the mini-tabs orthogonal to the wind direction may not be the most efficient way.

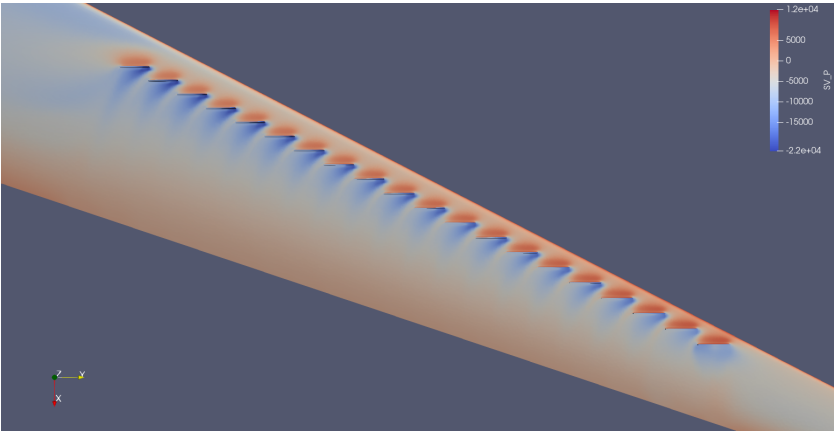


Figure 68: Surface pressure drag with $\theta = 0^\circ$ and AR = 10

The previous simulations showed that the gap between the mini-tabs had a negative impact on the performance in decreasing the lift coefficient. To eliminate the gaps that were present between the mini-tabs in the chordwise direction the next simulations were performed with the mini-tab rotated along the 20 percent chord line of the wing (figure 66c). Fig.69 shows the lift coefficient for different wall ratios and varying AR.

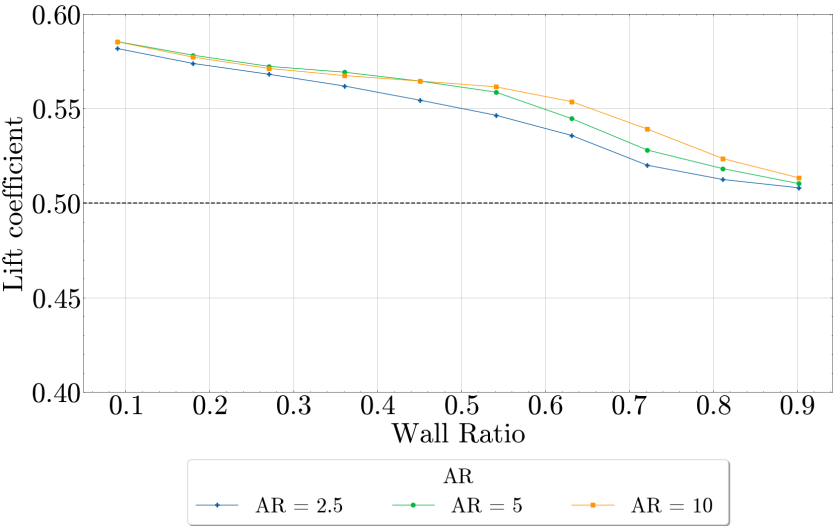


Figure 69: Lift coefficient for varying Wall ratio's and AR with $\theta = 25.6^\circ$

Figure 69 shows that for the case of the mini-tabs with $AR = 2.5$, the lift coefficient reduces faster than for the other cases. The reason for this is that to have the same wall ratio more tabs are placed on the wing reducing the distances between the mini-tabs. This will create a more uniform barrier that increases the separated flow downstream of the mini-

tabs. This will reduce the lift more when compared to the other cases as indicated in Fig.69.

For high wall ratios however, the differences between the lift coefficients of the mini-tabs with different AR should be reduced since the distances between the mini-tabs get smaller even for high aspect ratios. Fig.69 not only shows that for a wall ratio of 0.9, the differences are indeed small between the cases but also that the lift coefficients are converging towards the dotted line of 0.5. This dotted line was the simulation with the continuous mini-tab that spans the whole area. This shows that this orientation of the mini-tabs with $\theta = 25.6^\circ$ is more efficient in reducing the lift than the simulations with $\theta = 0^\circ$.

Figure 70 shows the pressure on the surface of the wing with the mini-tabs. As can be observed there is a uniform high pressure region at the leading edge which indicates that the mini-tabs are acting as a single mini-tab.

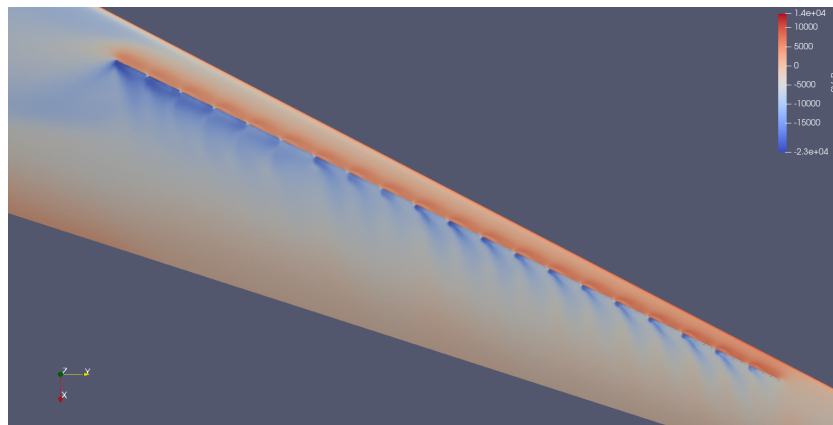


Figure 70: Surface pressure drag with $\theta = 25.6^\circ$ and AR = 10

Conclusion and Recommendations for Future Research

7.1. Conclusion

This thesis aimed to investigate the aerodynamic effect from the introduction of mini-tabs on the upper surface of a wing in subsonic and transonic conditions to determine their ability to alleviate the load. In the latter case, the wing DLR-F25 was used as a case-study. Through multiple RANS simulations, it was proved that the mini-tabs can effectively reduce the lift generated by a wing. This can be helpful when for example the airplane encounters a gust of wind. This will help to reduce the turbulence felt by the aircraft. This will reduce the loads and stress on the wing of an aircraft which can reduce the deformation and fatigue failure.

In the multiple mini-tabs configuration, a reduction of the lift coefficient of around 15 percent was observed compared to the original wing. By increasing the height and aspect ratio of the mini-tab the lift is reduced significantly and so does placing the mini-tab at around 60 percent of the chordwise position and closer to the tip. It was however observed that increasing the height, aspect ratio, spanwise location or chordwise position of the mini-tab also accelerates the flow at the lower surface of the wing.

The drag also increases with the reduction of the lift. While an increase of the drag may seem undesirable it can be useful at times. If for example, the airplane wants to turn to the right, by engaging the mini-tabs of the right wing the airplane will roll because of the difference in the lift generated by the wings. This will also increase the drag at the right side of the wing which will turn the airplane to the right. A normal airplane will use the ailerons to reduce the lift generated by the right and increase the lift of the left wing. This will cause a phenomenon called adverse yaw where the airplane will turn in the opposite direction which was intended due to the difference in drag generated by the wings. The use of the mini-tabs may prove to be more efficient than using the ailerons and rudder for the turning of the airplane.

Overall the results of this thesis prove that the mini-tabs have great potential as a load alleviation technique but also that caution needs to be taken in the designing of the mini-tabs since it can cause some unwanted effects like shockwaves. These strong differences in pressure can create vibrations which can affect the structural integrity of the airplane.

7.2. Recommendation for future research

To fully understand the aerodynamics around the mini-tabs further studies need to be done with transient simulations. This is particularly important because aerodynamic effects, like flow separation and reattachment which were found numerous times in the analysis of the mini-tabs, are often time-dependent and influenced by factors like turbulence and unsteady forces. By simulating these transient effects, a deeper understanding of how the flow interacts with the mini-tabs, leading to more accurate prediction of the performance of the mini-tab.

Another effect that was not taken into account in this thesis is a change in the angle of attack. When an aircraft encounters a gust of wind, the angle of attack changes which can increase the lift and the load on the wings. This change in the angle of attack can alter the performance of the mini-tab [10]. This should be investigated to have a better grasp on how this will effect the design of the mini-tabs.

Acknowledgments

The work presented herein has been partially funded by the European Community's Clean Aviation programme under the Grant Agreement 101101974. The UPWing project (Ultra-Performance Wing) is a project funded under the topic Climate, Energy and Mobility, involving 26 partners. The project started on January 1, 2023.

The DLR-F25 configuration that has been used for the initial design within the UP Wing project. The authors would like to thank the German Aerospace Center (DLR) for providing the DLR-F25 test case. The development of the DLR-F25 configuration is funded by the German Federal Ministry for Economic Affairs and Climate Action (BMWK) as part of the LuFo VI-2 project VIRENFREI (funding reference: 20X2106B).

Disclaimer

Co-Funded by the European Union. Views and opinions expressed are however those of the authors only and do not necessarily reflect those of the European Union or Clean Aviation Joint Undertaking. Neither the European Union nor the granting authority can be held responsible for them.

References

- [1] An Internet Book on Fluid Dynamics: Law of the Wall. <http://brennen.caltech.edu/fluidbook/basicfluidynamics/turbulence/>.
- [2] J. D Anderson. McGraw Hill, 2005.
- [3] Louis N. Cattafesta and Mark Sheplak. “Actuators for Active Flow Control”. In: Annual Review of Fluid Mechanics 43.1 (2011), pp. 247–272. DOI: [10.1146/annurev-fluid-122109-160634](https://doi.org/10.1146/annurev-fluid-122109-160634). URL: <https://doi.org/10.1146/annurev-fluid-122109-160634>.
- [4] D. J. Heathcote, I. Gursul, and D. J. Cleaver. “Aerodynamic Load Alleviation Using Minitabs”. In: Journal of Aircraft 55.5 (2018), pp. 2068–2077. DOI: [10.2514/1.C034574](https://doi.org/10.2514/1.C034574). URL: <https://doi.org/10.2514/1.C034574>.
- [5] D. J. Heathcote, I. Gursul, and D. J. Cleaver. “Aerodynamic Loads Alleviation Using Mini-tabs”. In: (2017).
- [6] K-Epsilon Turbulence Models. <https://www.simscale.com/docs/simulation-setup/global-settings/k-epsilon/>.
- [7] K-Omega Turbulence Models. <https://www.simscale.com/docs/simulation-setup/global-settings/k-omega-sst/>.
- [8] Yonghong Li and Ning Qin. “A Review of Flow Control for Gust Load Alleviation”. In: Applied Sciences 12.20 (2022). ISSN: 2076-3417. DOI: [10.3390/app122010537](https://doi.org/10.3390/app122010537). URL: <https://www.mdpi.com/2076-3417/12/20/10537>.
- [9] John C Lin. “Review of research on low-profile vortex generators to control boundary-layer separation”. In: Progress in Aerospace Sciences 38.4 (2002), pp. 389–420. ISSN: 0376-0421. DOI: [https://doi.org/10.1016/S0376-0421\(02\)00010-6](https://doi.org/10.1016/S0376-0421(02)00010-6). URL: <https://www.sciencedirect.com/science/article/pii/S0376042102000106>.
- [10] Luca Marino et al. “Parametric study of a switchable vortex generator for load alleviation in transonic conditions”. In: AIAA SCITECH 2024 Forum. DOI: [10.2514/6.2024-2110](https://doi.org/10.2514/6.2024-2110). eprint: <https://arc.aiaa.org/doi/pdf/10.2514/6.2024-2110>. URL: <https://arc.aiaa.org/doi/abs/10.2514/6.2024-2110>.
- [11] Keishi Nukina. Tour Report: Iranian SC Day 6 – Mahan Air A300-600 Iran Air A300B2. <https://knaviation.net/iran-air-a300b2-200-mahan-air-a300-600/>.
- [12] Chris Regan and Christine Jutte. “Survey of Applications of Active Control Technology for Gust Alleviation and New Challenges for Lighter-weight Aircraft”. In: (Apr. 2012).
- [13] SimScale: Mesh Quality. <https://www.simscale.com/docs/simulation-setup/meshing/mesh-quality/>.
- [14] The Spalart-Allmaras Turbulence Model. <https://turbmodels.larc.nasa.gov/spalart.html>.
- [15] Simon Thel et al. “A passive load alleviation aircraft wing: topology optimization for maximizing nonlinear bending–torsion coupling”. In: Structural and Multidisciplinary Optimization 65 (May 2022). DOI: [10.1007/s00158-022-03248-3](https://doi.org/10.1007/s00158-022-03248-3).
- [16] Neil Titchener and Holger Babinsky. “A review of the use of vortex generators for mitigating shock-induced separation”. In: Shock Waves (2015). ISSN: 0376-0421. DOI: <http://hdl.handle.net/1721.1/103353>. URL: <https://dspace.mit.edu/handle/1721.1/103353>.

- [17] Jia Xu and Ilan Kroo. "Aircraft Design with Active Load Alleviation and Natural Laminar Flow". In: 53rd AIAA/ASME/ASCE/AHS/ASC Structures, Structural Dynamics and Materials Conference. DOI: [10.2514/6.2012-1428](https://doi.org/10.2514/6.2012-1428). eprint: <https://arc.aiaa.org/doi/pdf/10.2514/6.2012-1428>. URL: <https://arc.aiaa.org/doi/abs/10.2514/6.2012-1428>.
- [18] Y plus wall distance estimation. https://www.cfd-online.com/Wiki/Y_plus_wall_distance_estimation.
- [19] Junwei Yang et al. "Experimental Study on Aerodynamic Characteristics of a Gurney Flap on a Wind Turbine Airfoil under High Turbulent Flow Condition". In: Applied Sciences 10.20 (2020). DOI: [10.3390/app10207258](https://doi.org/10.3390/app10207258). URL: <https://www.mdpi.com/2076-3417/10/20/7258>.